

¹ **MicroBooNE: Neutron Induced Cosmogenic π^0 's**

² **Ryan A.Grosso**

³ Submitted in partial fulfillment of the
⁴ requirements for the degree
⁵ of Doctor of Philosophy
⁶ in the Graduate School of Arts and Sciences

⁷ **UNIVERSITY OF CINCINNATI**

⁸ 2017

9

10

©2017

11

Ryan A.Grosso

12

All Rights Reserved

¹³ **Table of Contents**

¹⁴ **List of Figures**

¹⁵ **List of Tables**

¹⁶

Chapter 1

¹⁷

Introduction

¹⁸ This thesis describes work towards electromagentic shower reconstruction and steps towards
¹⁹ a neutral current single π^0 cross section measurement motivated from reconstruction tech-
²⁰ niques used for neutron induced cosmogenic π^0 analysis. This thesis will use data from
²¹ the MicroBooNE Liquid Argon Time Projection Chamber(LArTPC) located at the Fermi
²² National Accelerator in Batavia, Il.

²³

²⁴ To begin, Chapter ?? will provide some background about the neutrino. We will begin by
²⁵ presenting the initial premise for the need of a neutrino-like particle. Then, we will describe
²⁶ the theoretical framework used to address how they interact the standard model. Finally we
²⁷ will present the phenomenon known as neutrino oscillation and provide some mathematical
²⁸ framework to describe it. Chapter ?? begins with a brief history of the LArTPC detector
²⁹ technology and it's use as a high precision neutrino detector. The chapter continues to
³⁰ explain in depth the various subsystems that constitute the MicroBooNE detector. Chapter
³¹ ?? will describe how a neutrino beam is produced and delivered to the MircoBooNE detector.
³² It will focus on Fermilab's Booster Neutrino Beam(BNB) which generates a beam of nearly
³³ pure ν_μ or $\bar{\nu}_\mu$ around 1GeV in average energy. Chapter ?? will present in detail the claims
³⁴ of the electromagnetic ν_e -like excess first seen by the LSND experiment and then later
³⁵ verified by the MiniBooNE experiment. This chapter will also discuss the neutral current
³⁶ cross section, which is the main background in the MiniBooNE excess claim. Chapter
³⁷ ?? will introduce MicroBooNE's cosmogenic background and motivate the importance of

³⁸ understanding the cosmic rate. Here, we will also discuss the motivation to use cosmic
³⁹ π^0 events as a means of calibrating the detector energy scale. The cosmic backgrounds are
⁴⁰ addressed for the oscillation analysis and a future neutral current 1 π^0 measurement. Next,
⁴¹ this chapter will address simulation, reconstruction, and event selection. Chapter ?? will
⁴² present results from MicroBooNE cosmics data addressing the cosmic π^0 rate from neutral
⁴³ induced events.

⁴⁴

Chapter 2

⁴⁵

Neutrinos & Neutrino Oscillations

⁴⁶

2.1 The History the Neutrino

⁴⁷ The story of the neutrino began in Paris on a cloudy winter day in the year 1896. Parisian
⁴⁸ native, Henri Becquerel was experimenting with uranium salts and investigating the newly
⁴⁹ discovered x-ray radiation. [?] He hypothesized that when the salts were energized by sun-
⁵⁰ light they would produce the x-ray radiation. This hypothesis was disproven on the cloudy
⁵¹ February 27th day when his experiment still detected radiation emitting from the salts in
⁵² the absence of the sun. Becquerel had discovered radioactivity. In the coming years, this
⁵³ phenomena was supported by the work of Marie and Pierre Curie in studying the radioac-
⁵⁴ tivity of the element Thorium which lead to their discovery of the elements Polonium and
⁵⁵ Radium. These discoveries would later win Becquerel and the Currie's the 1903 Nobel Prize
⁵⁶ in Physics.

⁵⁷
⁵⁸ After radioactivity became an accepted phenomena in the science community, Ernst
⁵⁹ Rutherford discovered that radioactive decay products came in two different forms. He
⁶⁰ labeled them as α -decay and β -decay. At the time, beta decay was believed to be a two body
⁶¹ decay where a nucleus A decays into a lighter nucleus A' and a β -particle(electron). The
⁶² outgoing energy of the electron from a two body decay is given by equation ???. Assuming
⁶³ conservation of energy, the value of the outgoing energy should be a discrete.

$$E_e = \frac{m_A^2 + me^2 - m_{A'}^2}{2m_A} \quad (2.1)$$

64 In 1914, James Chadwick had discovered that the energy spectrum of the β -particles
 65 were continuations as opposed to mono-energetic. While some scientist were willing to
 66 abandon the requirement of energy conservation, others found this to be an unpalatable
 67 solution. Unable to attend the 1930 Tubingen physics conference in Germany, Wolfgang
 68 Pauli wrote a letter to the attendees in which he proposed the first idea of the neutrino.
 69 An excerpt from his famous December 4th letter is translated from German below [].

70 I have hit upon a desperate remedy to save the “exchange theorem” of statistics
 71 and the law of conservation of energy. Namely, the possibility that there could
 72 exist in the nuclei electrically neutral particles, that I wish to call neutrons,
 73 which have spin 1/2 and obey the exclusion principle and which further differ
 74 from light quanta in that they do not travel with the velocity of light. The
 75 mass of the neutrons should be of the same order of magnitude as the electron
 76 mass and in any event not larger than 0.01 proton masses. The continuous beta
 77 spectrum would then become understandable by the assumption that in beta
 78 decay a neutron is emitted in addition to the electron such that the sum of the
 79 energies of the neutron and the electron is constant...

80 In 1932, Chadwick discovered the neutron we know of today. Unfortunately, this neutron
 81 was too heavy to be the particle that Pauli had proposed. Expanding on Pauli’s work, Enrico
 82 Fermi proposed a more complete picture of beta decay and renamed Pauli’s ‘neutron’ to
 83 what is commonly called a *neutrino*. Fermi’s theory directly coupled the neutron with a
 84 final state proton, electron, and neutrino. This theory of beta decay, $n \rightarrow p + e^- + \bar{\nu}_e$
 85 preserves the law of conservation of energy and would later prove to be a more accurate
 86 descriptor the process.

⁸⁷ 2.2 Discovery of the Neutrino

88 Measuring and detecting neutrinos is a tricky business. In the 1950's, Clyde Cowan and
 89 Frederick Reines set out to directly measure neutrino interactions for the first time. If a free
 90 neutrino existed, they hypothesized that they could detect the byproducts from the inverse
 91 beta decay $\bar{\nu}_e + p \rightarrow e^+ + n$. They realized that such a measurement would require a very
 92 intense neutrino source and a large detector. Their first proposal, which was approved, was
 93 to detonate a nuclear bomb to supply the large, instantaneous source of neutrinos. A large
 94 detector filled with liquid scintillator would free fall down a mind shaft recording flashes
 95 of light from the ionizing positrons before landing on a bed of feathers and foam rubber.
 96 The original experimental schematic is shown in Figure ???. At that time, the theorized
 97 neutrino cross section was $10^{-43} \text{ cm}^2/\text{proton}$ while the existing measured limit was still 7
 98 orders of magnitude short in sensitivity. The bomb experiment would have worked but
 99 could not provide the level of sensitivity required to confirm detection for neutrino cross
 100 sections below $10^{-39} \text{ cm}^2/\text{proton}$. This was due to background interactions that came in
 101 time directly from the bomb.

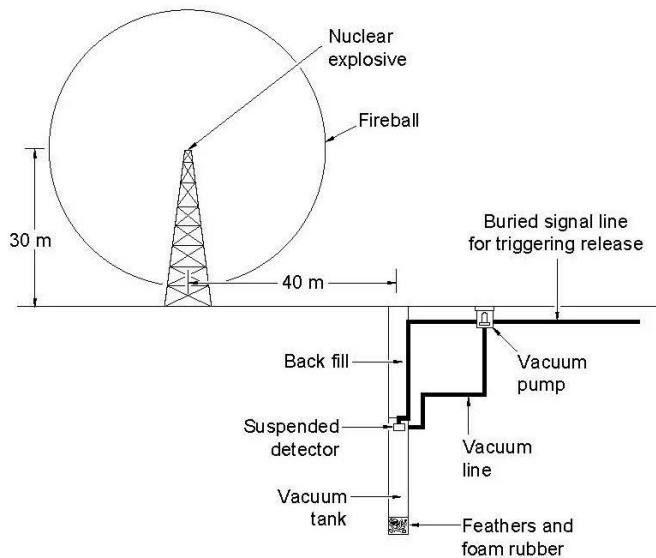
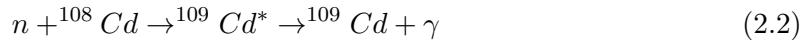


Figure 2.1: Original sketch of Cowan and Reines first proposed neutrino experiment.

Later, Reines realized tagging both the positron and neutron through a double coincidence would drastically reduce the backgrounds. This meant they could use a less intense neutrino source such as a nuclear reactor. They chose the Savannah River Plant near Augusta, Georgia which was estimated to produce neutrino fluxes on the order of $10^{12} - 10^{13}$ neutrinos/s/cm². The detector was composed of a water target that was doped with CdCl₂. As stated prior, the signal would rely on a double coincidence flash measured from photomultipiler tubes inside their detector. First, they would detect the positron as it annihilates with an electron via pair production ($e^+ + e^- \rightarrow \gamma + \gamma$). This is identified by two, back-to-back, coincident 0.511 MeV photons. Then, approximately 5μS later, a secondary photon would be detected which was produced from the neutron capture on Cadmium as shown in equation ??.



In 1956, only 25 years after Pauli's initial proposal of the neutrino, Cowan and Reines succeeded and provided the first direct experimental evidence of the electron flavor neutrino. In the subsequent years, the existence of two other flavors of neutrinos have been verified. In 1962, Lederman, Schwartz, and Steinberger discovered the ν_μ at Brookhaven Nation Laboratory by measuring neutrinos coming from pion decay. The ν_μ would be distinctly different from that of ν_e if the process $\nu_\mu + n \rightarrow p + e^-$ was forbidden. The results showed that the neutrinos from pion decay were indeed muon-like. Finally in 2000, the DONUT(Direct Observation of NeUtrino Tau) experiment stationed at Fermilab, made the first observed measurement of the ν_τ .

In 1956, C.S. Wu had shown that outgoing electron from beta decay maintained an opposing spin with respect to the spin of the parent nucleus. This turned out to be the first proof of maximal parity violation in weak interactions. Shortly thereafter, the neutrino helicity was first measured at Brookhaven National Labs by Maurice Goldhaber. In nature, neutrinos only have left handed helicity, while anti-neutrinos have right handed helicity. Helicity is frame dependent for particles with mass, which means there can be a reference frame in which the momentum vector can switch but the spin vector will not. For a

129 mass zero particles, this is not possible because the particle would already be traveling at
130 the speed of light. This assumption is what lead to the believe that neutrinos were massless.

131 The number of active light neutrinos are well constrained by studying the decay of the
132 Z^0 boson at LEP(Large Electron-Positron collider). LEP was an electron-positron collider
133 ring with a circumference of approximately 27 km that supported four primary experiments
134 (L3, ALEPH, OPAL and DELPHI). The facility was coined the phrase “Z-Factory” due
135 to it’s ability to record approximately 1000 Z^0 boson decays every hour during optimal
136 running conditions. The number of active neutrinos, N_ν is related to the width of the Z^0
137 resonance. Using 17 million Z^0 decays, LEP was able to show that $N_\nu = 2.9840 \pm 0.0082$

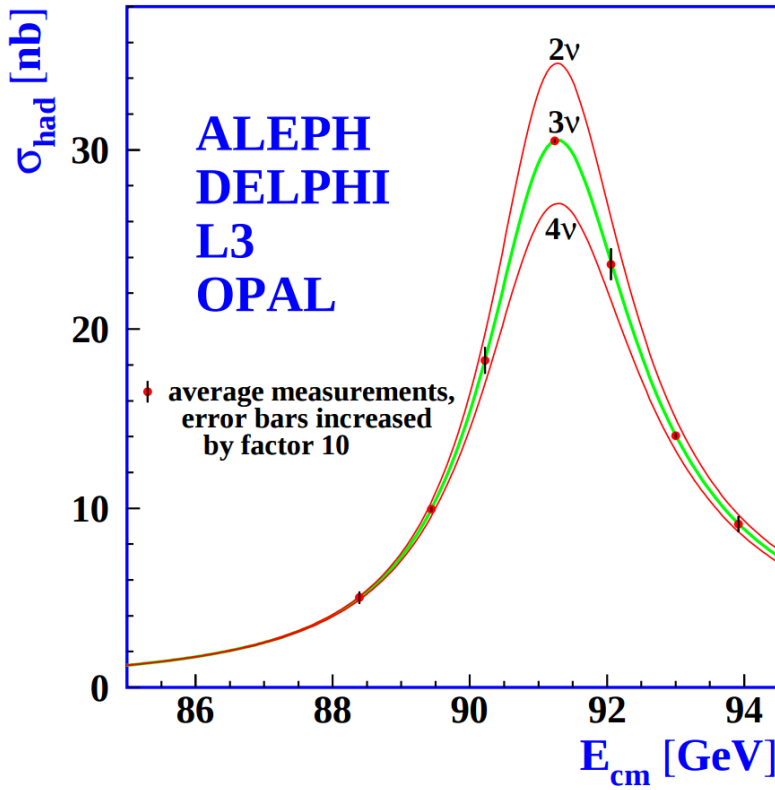


Figure 2.2: The Hadron production cross section around the Z^0 resonance from LEP. The curves for two, three, and four neutrino flavors are shown. The fit shows very compelling evidence of three active flavors of neutrinos.

¹³⁸ 2.3 Neutrinos in the Standard Model

¹³⁹ In the later half of the 20th century, scientists were looking for a way to describe all the
¹⁴⁰ fundamental forces and classify the known particles. The standard model of particle physics
¹⁴¹ is a phenomenological framework that describes the interaction of fundamental particles be-
¹⁴² tween the strong and electroweak forces. Having stood the test of time, the standard model
¹⁴³ accurately predicts most elementary particle interactions, but, does have it's limitations.
¹⁴⁴ The standard model does not account for gravity nor does it account for many new physics
¹⁴⁵ issues such as dark matter or dark energy. Most importantly, as we will see in section ??,
¹⁴⁶ it does not provide an accurate description of the neutrino.

¹⁴⁷ The standard model consists of two types of particles, bosons and fermions. The funda-
¹⁴⁸ mental bosons consist of two families: gauge bosons, which are typically the force carriers,
¹⁴⁹ and scalar bosons, which refer to spin zero particles or fields. The gluon, photon, and the
¹⁵⁰ weak boson are gauge bosons that mediate the strong, electromagnetic, and weak forces,
¹⁵¹ respectively. The Higgs boson is a scalar boson that possesses a nonzero vacuum expec-
¹⁵² tation value of 246GeV . This provides a mechanism for certain particles to gain mass
¹⁵³ even though their symmetries would suggest zero mass. The fundamental fermions are also
¹⁵⁴ divided into two families, quarks and leptons each having three generations. The quarks
¹⁵⁵ compose two main categories of particles, baryons and mesons. Baryons consist of an en-
¹⁵⁶ semble of 3 quarks. The most common and stable baryons in the universe are protons(uud)
¹⁵⁷ and neutrons(udd). Meson consist of an ensemble of quark anti-quark pairs and tend to
¹⁵⁸ have shorter lifetimes than their corresponding baryons. The lightest and most common
¹⁵⁹ mesons are pions($u\bar{d}, d\bar{u}, u\bar{u}/d\bar{d}$) and kaons($u\bar{s}, s\bar{u}, d\bar{s}/s\bar{d}$). The leptons are also divided into
¹⁶⁰ two families with three generations each. The charged leptons, most notably the electron,
¹⁶¹ interact via the strong and weak nuclear force and combine to form common baryonic mat-
¹⁶² ter. The neutral leptons are the neutrinos and only interact via the weak nuclear force.
¹⁶³ More details such as, mass, charge, and spin for various particles are shown in figure ??

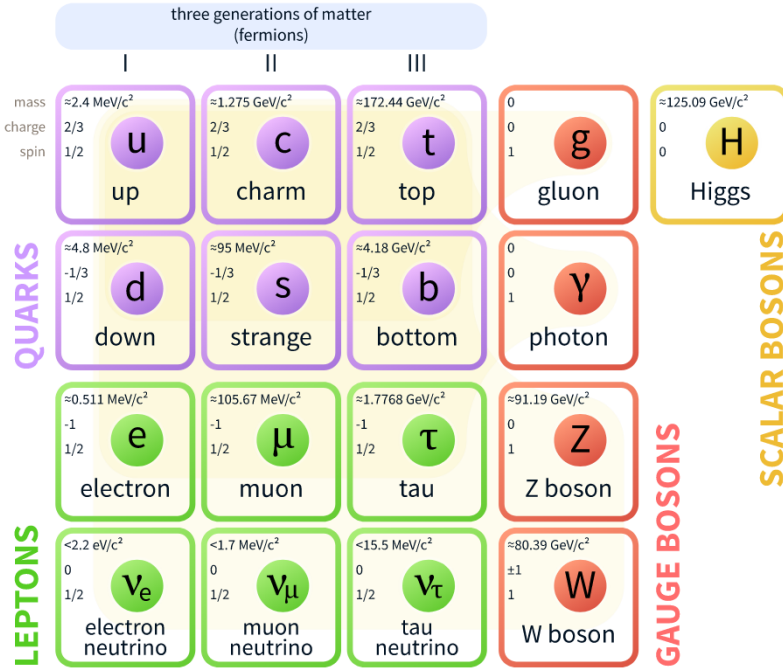


Figure 2.3: The current view of the standard model.

164 2.4 Neutrino Interactions

165 Neutrinos interact via the weak force. In the standard model, the weak force is unified
 166 with the electromagnetic force through an $SU(2) \otimes U(1)$ symmetry. The structure of the
 167 $SU(2)$ group symmetry accounts for the chirality of the fermion fields, along with ability to
 168 produce massive gauge bosons. The $U(1)$ group symmetry accounts for the massless photon
 169 propagator needed for electromagnetic interactions. For the quark and fermion families we
 170 define fermion fields in equations ?? and ?? , respectively. For formality we will define
 171 right(left)- handed neutrino(anti-neutrino) fields knowing that they will become irrelevant
 172 as the theory evolves:

$$\psi_1(x) = \begin{pmatrix} q \\ q' \end{pmatrix}_L , \quad \psi_2 = q_R , \quad \psi_3 = q'_R \quad (2.3)$$

$$\psi_1(x) = \begin{pmatrix} \nu \\ l \end{pmatrix}_L , \quad \psi_2 = \nu_R , \quad \psi_3 = l_R \quad (2.4)$$

173 We begin with the free Lagrangian, defined in equation ??, as it is already invariant in
174 flavor space.

$$\mathcal{L}_{\text{free}} \equiv \bar{\psi}(i\cancel{D} - m)\psi = i\bar{\psi}(x)\gamma^\mu\partial_\mu\psi(x) - m\bar{\psi}(x)\psi(x) \quad (2.5)$$

175 To make the Lagrangian invariant under local $SU(2) \otimes U(1)$, the fermion derivatives
176 have to be changed to covariant objects. This produces 4 different gauge parameters, shown
177 in equations ??, which correspond to the 4 different gauge fields required to describe the
178 W^\pm , Z^0 , and γ .

$$\begin{aligned} D_\mu\psi_1(x) &\equiv [\partial_\mu - ig\widetilde{W}_\mu(x) - ig'y_1B_\mu(x)]\psi_1(x) \\ D_\mu\psi_2(x) &\equiv [\partial_\mu - ig'y_2B_\mu(x)]\psi_2(x) \\ D_\mu\psi_3(x) &\equiv [\partial_\mu - ig'y_3B_\mu(x)]\psi_3(x) \end{aligned} \quad (2.6)$$

179 Where, σ^i are the Pauli spin matrices and B_μ represents a field imposed by an external
180 source. We find that,

$$\begin{aligned} \widetilde{W}_\mu(x) &\equiv \frac{\sigma_i}{2} \left\{ \partial_\mu W_\nu^i - \partial_\nu^i + g\epsilon^{ijk}W_\mu^jW_\nu^k \right\} \\ B_{\mu\nu} &\equiv \partial_\mu B_\nu - \partial_\nu B_\mu \end{aligned} \quad (2.7)$$

181 The Lagrangian now satisfies $SU(2) \otimes U(1)$ symmetry between all gauge fields as shown
182 in equation ???. It should be noted that the fermion fields and gauge bosons are required to
183 be massless. This does not accurately describe the true interaction since 3 of the 4 gauge
184 bosons are known to have mass, but the theory does allow an interface between neutrino
185 interactions in the standard model.

$$\mathcal{L} = \sum_{j=0}^3 i\bar{\psi}_j(x)\gamma^\mu D_\mu\psi_j(x) \quad (2.8)$$

186 From equation ??, the terms that account for interaction of gauge bosons with the
187 fermion fields are shown below in equation ??

$$\mathcal{L} \rightarrow g\bar{\psi}_1(x)\gamma^\mu\widetilde{W}_\mu\psi_1(x) + g'B_\mu\sum_{j=0}^3 y_j\bar{\psi}_j(x)\gamma^\mu\psi_j(x) \quad (2.9)$$

188 From this, we are then able to construct the Lagrangian for both the charged and neutral
189 currents. The charge current Lagrangian is shown in equation ??.

$$\mathcal{L}_{CC} = \frac{g}{2\sqrt{2}} \left\{ W_\mu^\dagger [\bar{q}\gamma^\mu(1-\gamma_5)q' + \bar{\nu}\gamma^\mu(1-\gamma_5)\bar{l}] + \dots \right\} \quad (2.10)$$

190 The neutral current term in the Lagrangian contains gauge fields for both the Z boson
191 and photon, which can be broken into two terms to account for a non-zero Z boson mass
192 while leaving the photon massless through spontaneous symmetry breaking(SSB). This is
193 done through an arbitrary rotation, as shown in equation ??, where θ_w is known as the
194 Weinberg or weak mixing angle. This angle is important because it is the angle used to
195 rotate through SSB giving the Z boson its mass.

$$\begin{pmatrix} W_\mu^3 \\ B_\mu \end{pmatrix} = \begin{pmatrix} \cos \theta_w & \sin \theta_w \\ -\sin \theta_w & \cos \theta_w \end{pmatrix} \times \begin{pmatrix} Z_\mu \\ A_\mu \end{pmatrix} \quad (2.11)$$

196 It is then possible to write the neutral current Lagrangian that accounts for the inter-
197 action of the Z boson as shown in equation ??.

$$\mathcal{L}_{NC} = \frac{e}{2\sin(\theta_w)\cos(\theta_w)} Z_\mu \sum_f \bar{f}\gamma^\mu(v_f - \alpha_f\gamma_5)f \quad (2.12)$$

198 where,

$$g\sin(\theta_w) = g'\cos(\theta_w) = e \quad \text{and} \quad \cos(\theta_w) = \frac{M_w}{M_z} \quad (2.13)$$

199 The neutral current coupling constants, v_f & α_f , differ with respect to the various quark,
200 charged and neutral lepton fields. The neutrinos can be described as interactions via the
201 charged and neutral currents. The Feynman diagrams, shown in figure ??, depict how the
202 leptons couple to the quarks via the current mediator.

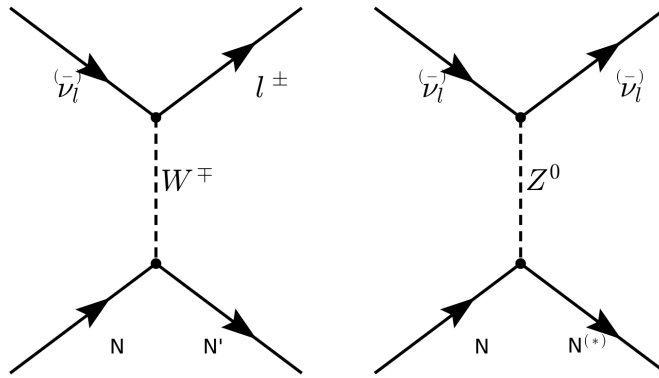


Figure 2.4: The Feynman diagram on the left describes a charged current(CC) neutrino interaction which transforms neutrinos into their corresponding charged leptons. In the CC interaction diagram the $N \rightarrow N'$ represents a changed nucleon charge. The diagram on the right shows the neutral current(NC) neutrino interaction with preserves the neutrino while it interacts. In the NC intearction diagram the $N \rightarrow N^*$ represents a same charge nucleon that could be at a higher resonance state.

2.5 Neutrino Mass and Flavor Oscillations

Neutrino oscillation is a quantum mechanical phenomenon in which the fraction of neutrino flavor changes while it propagates. This phenomena was first proposed in 1957 by Bruno Pontecorvo and relates the neutrino mass eigenstates with the flavor eigenstates through a rotation. This phenomena is best shown through a two neutrino flavor example, then extended into 3 flavors.

The mixing matrix for a two flavor neutrino case is:

$$\begin{pmatrix} \nu_e \\ \nu_\mu \end{pmatrix} = \begin{pmatrix} \cos \theta & \sin \theta \\ -\sin \theta & \cos \theta \end{pmatrix} \begin{pmatrix} \nu_1 \\ \nu_2 \end{pmatrix} \quad (2.14)$$

In this example, the flavor states are represented as ν_e and ν_μ which are expressed as a mixture of mass states ν_1 and ν_2 . For ascetic reasons, we chose ν_μ to be part of the example because most man made neutrino beams produce a relative pure sample of ν_μ . The framework for this example is commonly used as an oscillation approximation and can be generalized to satisfy any case of two distinctly different flavor neutrinos.

²¹⁵ Using the two flavor formalism a pure ν_μ neutrino state can be expressed as equation
²¹⁶ ??

$$|\nu_\mu(0)\rangle = -\sin \theta |\nu_1(0)\rangle + \cos \theta |\nu_2(0)\rangle \quad (2.15)$$

²¹⁷ The evolution of the state is governed by solving the time dependent Schroedinger
²¹⁸ equation for the initial muon state:

$$|\nu_\mu(t)\rangle = e^{-i\frac{Et}{\hbar}} |\psi(0)\rangle = -e^{-i\frac{E_1 t}{\hbar}} \sin \theta |\nu_1\rangle + e^{-i\frac{E_2 t}{\hbar}} \cos \theta |\nu_2\rangle \quad (2.16)$$

²¹⁹ Assuming neutrinos travel near the speed of light, we rewrite equation ?? using the
²²⁰ relativistic approximation, along with setting $c = \hbar = 1$ and $p_1 = p_2 = p$:

$$|\nu_\mu(t)\rangle \simeq -e^{-i(p_1 + \frac{m_1^2}{2p_1})t} \sin \theta |\nu_1\rangle + e^{-i(p_2 + \frac{m_2^2}{2p_2})t} \cos \theta |\nu_2\rangle \quad (2.17)$$

²²¹ with,

$$E = \sqrt{p^2 + m^2} = p \sqrt{1 + \frac{m^2}{p^2}} \approx p + \frac{m^2}{2p} \quad (2.18)$$

²²² Next, the mass terms are grouped together and defined as the absolute square difference,
²²³ $\Delta m^2 \equiv |m_2^2 - m_1^2|$. We find that if the mass are different then the mass eigenstates propagate
²²⁴ at different frequencies and give rise the oscillatory behavior. The time dependent state can
²²⁵ now be wrote as:

$$|\nu_\mu(t)\rangle = e^{-i\phi} (-\sin \theta |\nu_1\rangle + e^{+i\frac{\Delta m^2}{2p} t} \cos \theta |\nu_2\rangle) \quad (2.19)$$

with, $e^{-i\phi} \equiv e^{-i\left(p + \frac{m_1}{2p}\right)t}$

²²⁶ To calculate the probability of the initial ν_μ state being measured as a ν_e state at some
²²⁷ later time t , we need to calculate the absolute value squared of the overlap between the
²²⁸ states. Utilizing the relationship $\langle \psi_i | \psi_j \rangle = \delta_{ij}$, the overlap between the states is:

$$\langle \nu_e | \nu_\mu(t) \rangle = e^{-i\phi} (-\sin \theta \cos \theta + \sin \theta \cos \theta e^{i\frac{\Delta m^2}{2p} t}) \quad (2.20)$$

²²⁹ The probability reduces to:

$$\begin{aligned}
 P(\nu_\mu \rightarrow \nu_e) &= |\langle \nu_e | \nu_\mu(t) \rangle|^2 \\
 &= e^{i\phi} e^{-i\phi} \sin^2 \theta \cos^2 \theta (-1 + e^{-i\frac{\Delta m^2}{p}t})(-1 + e^{+i\frac{\Delta m^2}{p}t}) \\
 &= \frac{1}{2} \sin^2 2\theta \left(1 - \cos \left(\frac{\Delta m^2}{2p} t \right) \right)
 \end{aligned} \tag{2.21}$$

²³⁰ Finally, from relativistic assumptions, we set $p = E_\nu$ as the outgoing neutrino energy
²³¹ and $t = L$ corresponds to the distance traveled.

$$P(\nu_\mu \rightarrow \nu_e) = \sin^2 2\theta \sin^2 \left(\frac{\Delta m^2 L}{4E_\nu} \right) \tag{2.22}$$

²³² From a proper accounting of numerical values of c and \hbar , equation ?? is more commonly
²³³ written as:

$$P(\nu_\mu \rightarrow \nu_e) = \sin^2 2\theta \sin^2 \left(1.27 \frac{\Delta m^2 L}{E_\nu} \right) \tag{2.23}$$

²³⁴ This oscillation behavior is best visualized as a plot of the probability of appearance
²³⁵ and disappearance as shown Figure ??.

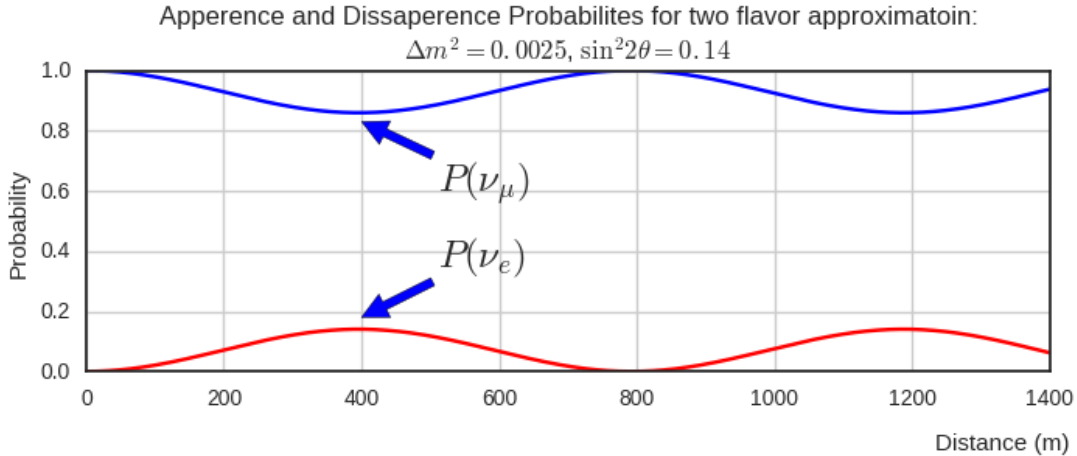


Figure 2.5: This plot shows the appearance and disappearance curves for a 2-flavor approximation as a function of baseline. The values of $\Delta m^2 = 0.0025 \text{ eV}^2$ and $\sin^2 \theta = 0.14$ are used.

As shown prior from figure ??, there are very good constraints on the number of active neutrinos. Extending this formalism to a 3 flavor case was done by Pontecorvo-Maki-Nakagawa-Sakata (PMNS). The PMNS matrix is a 3 dimensional unitary matrix which is parameterized by three mixing angles $\theta_{12}, \theta_{23}, \theta_{13}$ a complex phase δ . The three angle correspond to the mixing effect, while δ is known as the charge parity(CP) phase. If the CP-phase is non-zero, then neutrinos violate charge parity conservation which leads to the conclusion that neutrinos and anti-neutrinos interact differently with matter. The value for δ has yet to be observed.

$$U_{PMNS} = \begin{pmatrix} 1 & 0 & 0 \\ 0 & c(\theta_{23}) & s(\theta_{23}) \\ 0 & -s(\theta_{23}) & c(\theta_{23}) \end{pmatrix} \begin{pmatrix} c(\theta_{13}) & 0 & s(\theta_{13})e^{-i\delta} \\ 0 & 1 & 0 \\ -s(\theta_{13})e^{i\delta} & 0 & c(\theta_{13}) \end{pmatrix} \begin{pmatrix} c(\theta_{12}) & s(\theta_{12}) & 0 \\ -s(\theta_{12}) & c(\theta_{12}) & 0 \\ 0 & 0 & 1 \end{pmatrix} \quad (2.24)$$

where $c(\theta_{ij}) \equiv \cos \theta_{ij}$ and $s(\theta_{ij}) \equiv \sin \theta_{ij}$. The matrix equation is now put into a more compact manor that relates the mixing of the 3 neutrino generations.

$$\begin{pmatrix} \nu_e \\ \nu_\mu \\ \nu_\tau \end{pmatrix} = \begin{pmatrix} U_{e,1} & U_{e,2} & U_{e,3} \\ U_{\mu,1} & U_{\mu,2} & U_{\mu,3} \\ U_{\tau,1} & U_{\tau,2} & U_{\tau,3} \end{pmatrix} \begin{pmatrix} \nu_1 \\ \nu_2 \\ \nu_3 \end{pmatrix} \quad (2.25)$$

In it's most general form, the oscillation probability is:

$$P(\nu_\alpha \rightarrow \nu_\beta) = \delta_{\alpha,\beta} - 4 \sum_{j>i} U_{\alpha,i} U_{\beta,i} U_{\alpha,j}^* U_{\beta,j}^* \sin^2 \left(1.27 \frac{\Delta m_{ij}^2 L}{E_\nu} \right) \quad (2.26)$$

From equation ??, we see that the oscillation probability is depended on the mass difference between states. There is currently no method to directly measure the mass of any given neutrino. Therefore, there is an allowed ambiguity in the mass ordering of all three neutrino states. This is called the neutrino hierarchy problem. However, we do know that the difference between m_1 and m_2 is small relative to m_3 . Using this, we can build a picture of the fraction of different flavor eigenstates corresponding to their various mass states for both types of hierarchy.

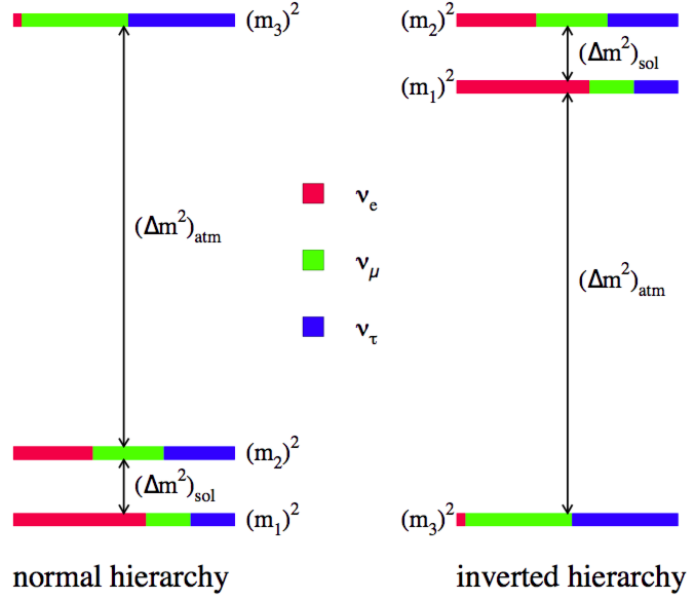


Figure 2.6: The two possible ordering for the 3 active neutrino mass eigenstates.

Many experiments have measures various elements of the PMNS matrix with neutrinos coming from accelerators, reactors, and solar sources. Currently, normal hierarchy ($m_1 < m_2 < m_3$) is favored, therefore we will show (table ??) the current Particle Data Group(PDG)[1] best fit values for oscillation parameters with respect to normal hierarchy.

$$\begin{aligned}
 \Delta m_{21}^2 &= 7.37 \times 10^{-5} eV^2 \\
 \Delta m_{32}^2 &= 2.50 \times 10^{-3} eV^2 \\
 \sin(\theta_{12}) &= 0.297 \\
 \sin(\theta_{23}) &= 0.437 \\
 \sin(\theta_{13}) &= 0.0214 \\
 \delta/4 &= 1.35
 \end{aligned} \tag{2.27}$$

258 **2.6 Sterile Neutrinos**

259 It is well accepted, from measurements at LEP[], that there are only 3 neutrinos that couple
260 through the weak interaction. Mathematically, nothing prohibits a theory that allows for
261 neutrino mixing with other neutrino states beyond the 3 active states. These states, since
262 they do not interact weakly, are called 'sterile neutrinos'. Extending the 3 flavor oscillation
263 model to include any number of sterile neutrinos may be a possibility to address some the
264 currently unexplained results in the neutrino physics fields. Each additional state requires
265 an extra dimension to be added to the PMNS matrix. The sterile eigenstates are then
266 defined as

$$|\nu_{s_i}\rangle = \sum_j^{3+N} U_{s_i,j} |\nu_j\rangle \quad (2.28)$$

267 where N is the number of sterile neutrinos. The necessity for additional sterile neutrinos
268 was prompted by the LSND experiment and later supported by the MiniBooNE. experiment.
269 Both experiments are explained in depth in chapter ???. Each experiment found an excess
270 of electron-like events at low energy. This suggested a Δm^2 parameter space observed to
271 be 1eV^2 larger than expected and strongly contradicted the results of many other results
272 which had Δm^2 around $\mathcal{O}(10^{-3}\text{eV}^2)$ and $\mathcal{O}(10^{-5}\text{eV}^2)$. This precipitated the need for
273 further exploration of the LSND and MiniBooNE claims with more sophisticated detector
274 technologies. The MicroBooNE experiment was proposed in 20071 and will be the focal
275 point for this thesis.

276 Chapter 3

277 The MicroBooNE Detector

278 3.1 Brief History of LAr-TPC's

279 The surprising nature of neutrinos quickly prompted the need for precision measurements
280 of their interactions. Unfortunately, the low neutrino cross section posed a hurdle to build
281 a high statistics detector. In 1977, C.Rubbia propose a Liquid Argon Time Projection
282 Chamber (LArTPC) as large, high precision neutrino detector.^[1] In 2001, The ICARUS col-
283 laboration commissioned the T600 detector which was one of the first large scale LArTPC's
284 to be used as a neutrino detector. ^[2] The T600, which is comprised 760 tons of liquid argon
285 and commissioned in Pavia, Italy using cosmic rays as a proof of principle. Later the T600
286 was place underground in Hall B of Laboratori Nazionali del Gran Sasso (LNGS) which is
287 located 730 km from the source of the CERN neutrino beam.

288 In 2009, the AgroNeut collaboration, commissioned a small LArTPC in a 175 liter
289 vacuum jacketed cryostat. The ArgoNeut TPC was comprised of 3 wire planes and operated
290 at a drift field of 500 V/cm. The detector was placed just in front of the MINOS near
291 detector in the NuMI beam at Fermi National Accelerator Laboratory(FNAL)^[3]. AgroNeut
292 collected thousands of neutrino and antineutrino events providing valuable physics data and
293 detector R&D for future experiments with LArTPC's.

294 The MicroBooNE (the Micro Booster Neutrino Experiment) detector, which will be
295 discussed in depth throughout this chapter, is the first multi-ton LArTPC to be fully op-
296 erational in the U.S. The MircoBooNE detector design pioneered many new detector R&D

297 concepts such as: the ability to maintain high LAr purity in an unevaluated vessel, imple-
 298 mentation of low noise electronic readouts at liquid cryogenic temperatures and advances
 299 in reconstruction techniques. MicroBooNE also, supports a robust, high statistics physics
 300 program to address the MiniBooNE Low Energy Excess and various cross section measure-
 301 ments. MicroBooNE was commissioned and began taking cosmic ray data in the summer of
 302 2015. In October 2015 it began taking neutrino data. Shortly there after, the first neutrino
 303 event candidates were identified. []

304 3.2 Introduction

305 The MicroBooNE detector utilizes 170 tons of liquid argon to sustain 87 tons of active
 306 detector mass. It is located at the Liquid Argon Test Facility (LARTF) which is 470
 307 m downstream of the Booster Neutrino Beam-line(BNB) source at the Fermilab National
 308 Accelerator Lab (FNAL) in Batavia, Illinois. The detector is the first large scale LArTPC
 309 to be deployed, commissioned and fully operated in the US.

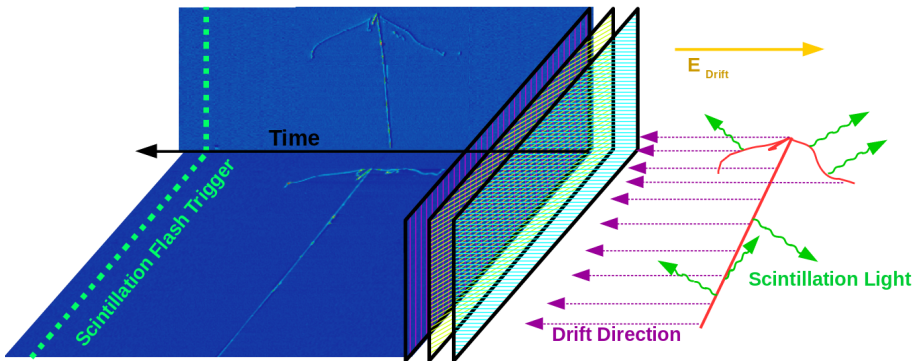


Figure 3.1: This diagram explains how a TPC works. First, charged tracks ionize the argon. The remaining ions produce prompt scintillation light and the corresponding electrons begin to drift towards the wires due to the presence of the electric field. When the drift electrons reach the wire planes a 2D image is produced for each plane. When combining the 2D images from multiple planes along with the scintillation light information a 3D reconstruction is possible.

310 The general principle of a LArTPC involves utilizing two properties of LAr, scintillation

311 light and ionization. Charged particles travel through the argon and produce scintillation
312 light which is collected by photomultiplier tubes (PMT's). A uniform electric field is applied
313 over active volume which transports the ionization electrons to a series of wire planes.
314 Assuming the argon is pure and has minimal electro-negative contaminants, the wire planes
315 then measure the induced or collected charge signal from the drifting electrons. The planes
316 are each oriented at a different pitch angles. Each plane then can then produce a two
317 dimensional image of the event as a function of wire and time. Combining multiple planes
318 along with the PMT information allows for the object to be fully reconstructed in three
319 dimensions. A diagram of the TPC concept is show in Figure ???. In the following sections
320 the TPC, light collection system, and electronics are described in detail.

321 **3.3 Time Projection Chamber**

322 The TPC is the core of the MicroBooNE detector and forms a rectangular prism with
323 dimensions $2.3m \times 2.6m \times 10.4m$ which contains 87t of LAr. The longest dimension, which
324 in MicroBooNE's coordinate system is referred to as the z-direction, is oriented on axis
325 of the BNB. The majority of the TPC materials are composed of 304V stainless steel
326 and G10. Stainless steel was chosen due to it's low magnetic susceptibility, resistance to
327 corrosion/oxidation, and ability to maintain it's strength in cryogenic temperatures. G10
328 was chosen due to it's ability to perform well as an insulator in cryogenic environments.



Figure 3.2: The MicroBooNE TPC is shown here. On the far right is the flat cathode plane. The far left shows the 8,456 anode wires installed. The field cage tubes, which provide the uniform electric field, span the length between the anode and cathode.

329 The TPC field cage, which provides the uniform electric field through the detector
 330 volume, and was designed to produce field strengths up to 500 v/cm in liquid argon. The
 331 field cage consists of a total of 64 stainless steel rectangular loops that are supported and
 332 evenly spaced by a G10 holder. The cathode plane is a series flat stainless steel sheets that
 333 is opposite the anode sense wires. Figure ?? shows the MicroBooNE TPC.

334 Every piece that was used in the MicroBooNE detector was thoroughly cleaned. Many
 335 pieces were cleaned in an ultrasonic cleansing bath while others were cleaned by hand.
 336 The detector was constructed in a clean environment that maintained positive pressure to
 337 mitigate the accumulation of dust. A complete description of the process is summarize in
 338 a separate technical note. []

339 MicroBooNE has a total of 8,265 sense wires that form 3 unique wire planes, one vertical
 340 collection plane (Y) and two induction planes (U,V) oriented at ± 60 relative the Y plane.
 341 The wire planes are separated by 3 mm. The wires in each plane are evenly spaced by 3
 342 mm pitch on carrier boards. The Y plane consists of 3,456 wires with a total of 108 carrier
 343 boards that accommodate 32 wires each. Each of the U and V planes consist of 2,400 wires
 344 with a total of 150 carrier boards that accommodate 16 wires each. The wires themselves
 345 are made of 304V stainless steel and are $150 \pm 5\mu\text{m}$ in diameter. A $2\mu\text{m}$ layer of copper
 346 is plated over the wires to decrease the resistivity from $40\Omega/\text{m}$ to $3\Omega/\text{m}$. The reduced

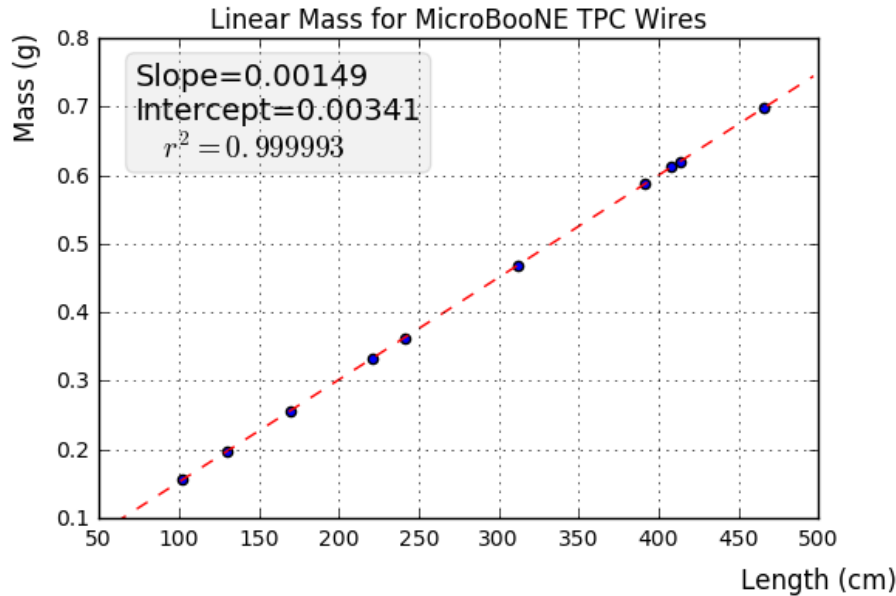


Figure 3.3: This plot is for a small sample used to cross check the linear mass density measured from the wire dealer. The slope from this plot represents the linear mass density and was found to be consistent with the value 0.149g/m

347 resistivity aids in noise reduction at cryogen temperatures. Finally the wire is covered in
 348 and outer layer 0.1 μ m of gold to prevent the copper from oxidizing over time. The linear
 349 mass density of a small sample of wires was measured and is shown in figure ??.

350 The wires were designed to installed at a nominal tension of 6.97 N. To account for this,
 351 the carrier boards were installed onto a series of tensioning bars on the anode frame. These
 352 tensioning system, as shown in figure ??, allowed for fine tune adjustments to be made to
 353 separate sections of wires.

354 There are a total of 12 tensioning bars, 2 sets of 5 that traverse the entire top and bottom
 355 length of the anode frame, and 2 spanning the entire height of the upstream and downstream
 356 sections of the anode frame. Bronze jacking screws were used for final adjustments once
 357 all the wires were installed. Bronze was chosen since it has a similar thermal expansion
 358 coefficient to stainless steel and it is a softer metal which helps mitigate the risk of cold
 359 welding with stainless steel during the tensioning process.

360 In preparation for installing the actual detector wires, an installation team was trained

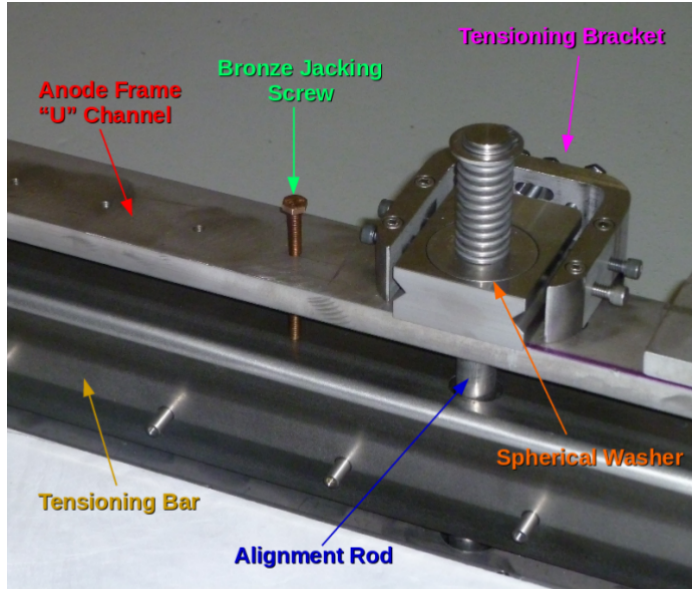


Figure 3.4: The MicroBooNE tension system. Wire carrier boards (not shown here) are mounted on the tensioning bar. The tensioning bar is able to move the wires during the tensioning process. Bronze jacking screws were used for final alignment during the tensioning process

361 on how to properly handle and install them. A 'mock-wire' installation was done to practice
 362 and identify the risks. After this, the actual wires were installed. The installation took
 363 approximately one week. The wires were installed serially, first the Y-plane, then the U-
 364 plane, and then the V-plane. After all the wires were install, a G10 cover board was placed
 365 over carrier boards to secure and protect the electronics on the board, as shown in figure
 366 ??.

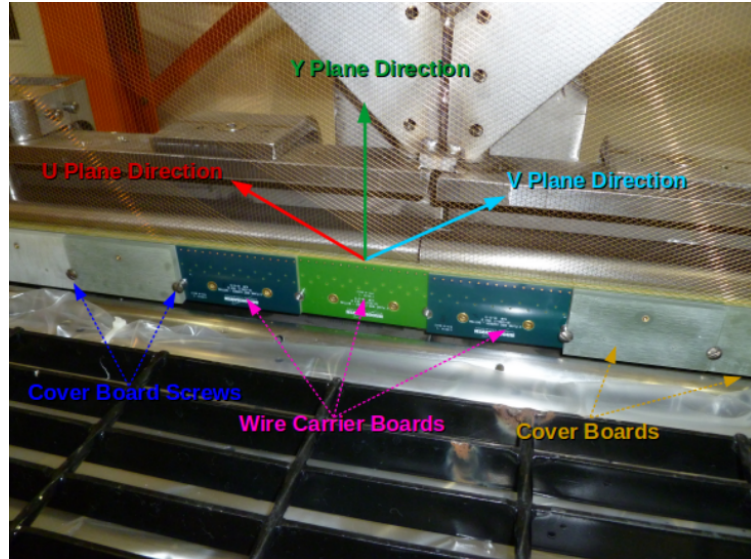


Figure 3.5: The MicroBooNE wires for 3 planes are shown here. The wire carrier boards are serially installed on the tensioning bar. The boards are held in place with a G10 cover plate that is secured with a smooth stainless steel screw.

367 Next, the wires were brought as close to nominal tension as possible. It was decided to
 368 favor under tensioning wires to minimize the risk of a broken wire during the tensioning
 369 process. The wire tensioning was done in a systematic way using the bronze jacking screws.

$$f = \frac{1}{2L} \sqrt{\frac{T}{\rho}} \quad (3.1)$$

370 Each wire has a characteristic resonance frequency that is related to its length, tension,
 371 and linear mass density through equation ???. A custom device was made to measure
 372 the resonant frequency of individual MicroBooNE wires. A laser light was focused on a
 373 particular wire and the wire gently plucked. A photo-diode mounted in an optical lens then
 374 measured the intensity of reflected light as the wire vibrated. The signals were then read into
 375 SpectrumAnalyzer, which is a software package that records frequency. SpectrumAnalyzer
 376 also allowed the high order frequency harmonics to be seen. The higher frequencies allowed
 377 for more precise tension measurement as see in Figure ???

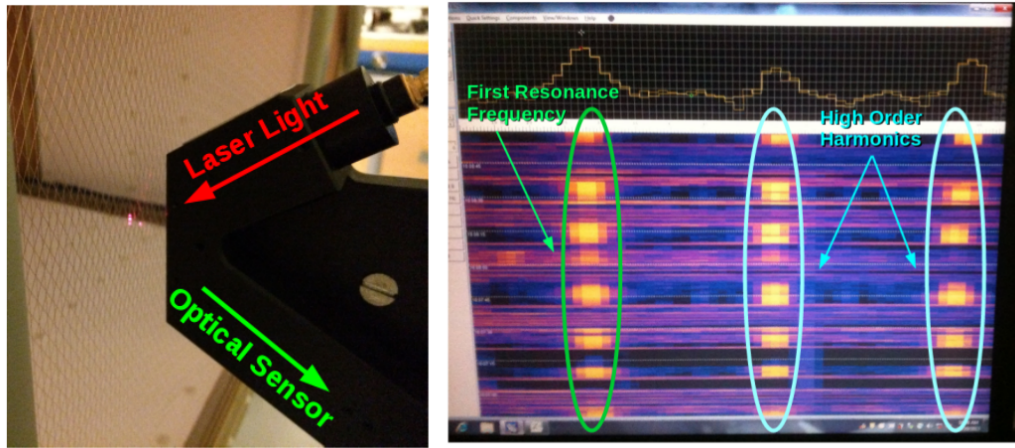


Figure 3.6: Left: Picture of the tension measuring apparatus including a laser and a optical sensor made of a photo-diode and a lens. Right: Example output of the SpectrumAnalyzer showing the first resonance frequency (bright line on the left) and the higher order harmonics (lines in the middle and left).

378 Note that the tension of 2328 out of 2400 U wires, 2308 out of 2400 V wires, and 3410
 379 out of 3456 Y wires was measured, corresponding to 97.5 % of all wires installed in the
 380 detector. Only the wires inaccessible to the tension measuring device were not measured.
 381 The average tension for U,V,Y planes respectively was 0.589 ± 0.012 kg, 0.664 ± 0.014 kg,
 382 0.525 ± 0.009 kg. The tension for each plane is shown in Figure ?? and Figure ??.

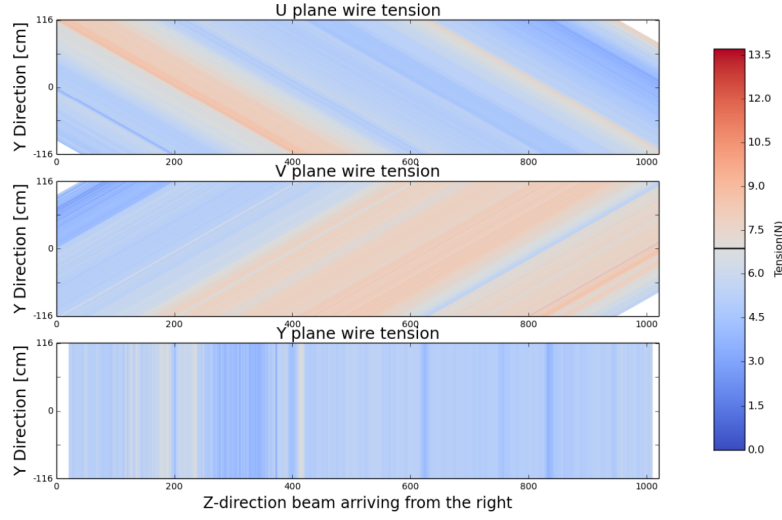


Figure 3.7: This a plane by plane map of the measured wire tensions for MicroBooNE.

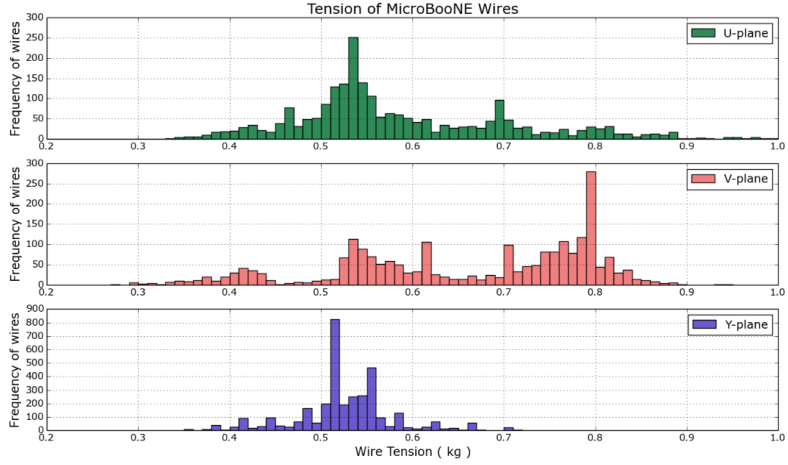


Figure 3.8: This a plane by plane histogram of the measured wire tensions for MicroBooNE.

3.4 Light Collection

The TPC can reconstruct 3D objects but there is still an ambiguity in the initial drift position. The light collection system in an LArTPC provides information to address this degeneracy. Scintillation light of liquid argon is 128nm wavelength and is produced through two primary reactions. The first, which accounts for $\approx 25\%$ of the light yield, is done through a Σ singlet excimer excitation and has a reaction time of 6 ± 2 ns. This type of

389 excimer is formed from an ionized argon atom that combines with another stable argon
 390 atom. The second, which accounts for the other 75% of light yield, is done through a Σ
 391 triplet excimer excitation and has a reaction time of $1590 \pm 100 \mu\text{s}$. The triplet state excimer
 392 is formed from a stable argon atom, an ionized argon atom, and a free electron.^[1] Since the
 393 prompt scintillation light is orders of magnitude faster than drift time from the TPC signal
 394 this information can be used to address this ambiguity.

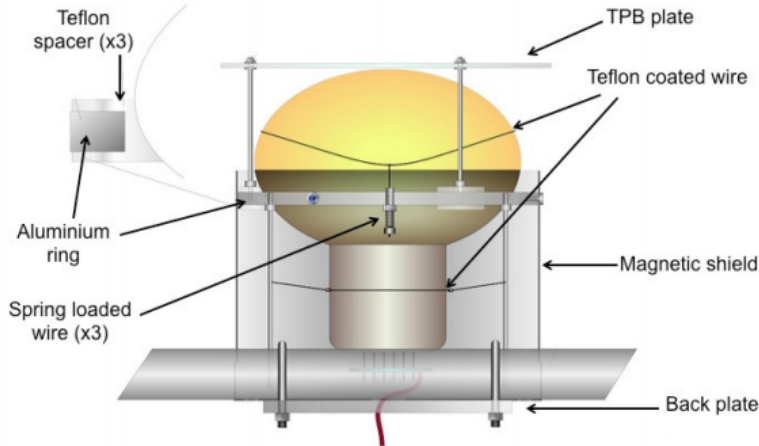


Figure 3.9: Schematic of a PMT optical unit for MicroBooNE.

395 The MicroBooNE light collection system consists of 32 8-inch diameter Hamamatsu
 396 R5912-02mod cryogenic PMTs. The PMT's are not optimized to detect 128nm vuv light.
 397 Therefore, an acrylic plate coated with tetraphenyl butadiene(TPB)^[2] was installed in front
 398 of the PMT's to act as a wavelength shifter. The TPB plate absorbs the 128nm light and
 399 re-emits it a peak wavelength of 425nm. Also, it is known that PMT response is reduced
 400 from certain orientations in the earth magnetic field. To address this a mu-metal shield was
 401 designed to extend just past the equator of the PMTs. A schematic of a PMT optical unit
 402 is shown in figure??.

403 The PMT system is mounted on a railing behind the wire planes and spans the entire
 404 detector length as shown in figure ???. This also provides a weak handle on interaction
 405 position since the scintillation light is fairly localized. Most importantly, since MicroBooNE
 406 is a surface detector and constantly being bombarded by cosmic rays, the scintillation flash

407 is used as a method of identifying neutrino interactions coming in time with the beam.



Figure 3.10: PMT optical units installed on support racks inside the MicroBooNE cryostat

408 3.5 Electronics Readout

409 The TPC and PMT systems produce detector analog signals which need to be digitized,
410 transferred out of the detector, and written to disk through data acquisition(DAQ) software.
411 Both systems perform a first round of shaping and amplification in the cold LAr and then
412 interface with warm electronics for further processing. The DAQ continuously writes to disk
413 and creates a buffer which stores data for up to 24 hours. MicroBooNE employs various
414 triggers to signify beam and non-beam data blocks and permanently store data from the
415 buffer stream. A schematic overview of the TPC and PMT signal processing and readout
416 stages is shown in Figure ??.

417 For the TPC, a large portion of the electronics processing for the 8,256 wire signals
418 are performed directly in the LAr. To reduce electronics noise, the input distance from
419 the wires to the preamplifier is minimized. The sense wires directly interface with CMOS
420 analog front end ASICs which operate on cold motherboards. In total MicroBooNE has
421 516 CMOS ASICs. The ASICs generate 50 W of heat load which is a negligible impact on
422 the cryogenics system. The motherboards shape and amplify the low noise signal. There

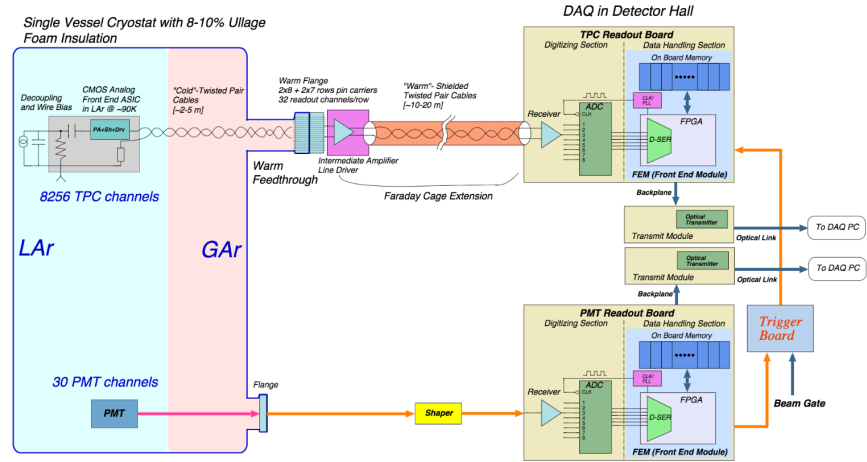


Figure 3.11: MicroBooNE LArTPC and PMT signal processing and readout schematic.

423 are 36 top style motherboards that instrument Y,U and V plane wires and 14 side style
 424 motherboards that instrument U and V plane wires. The signals are then passed through a
 425 series of 12 feedthrough ports to warm electronics. The warm signals are then distributed
 426 over nine readout crates, which digitize the signals.

427 The TPC system read out frame is defined to be 1.6 ms. This number was chosen
 428 to account for ionization electrons that are generated at the cathode and drift the entire
 429 distance to the wires in the presence of a 500V/cm E-Field. In MicroBooNE, an event is
 430 defined as four 1.6 ms readout frames. The additional frames allow for identification of
 431 cosmic particles that arrive before and after the neutrino interaction.

432 The PMT system is also processed in a similar fashion. The PMT's undergo 60 ns
 433 shaping to allow for precise measurements of the signal rising edge. The signals are sampled
 434 at 64MHz but only shaped signals above a threshold are read out and stored for data. The
 435 PMT signals are split into two different gains. A high gain signal that is 10 times the
 436 amplitude of the low gain. The signals are then brought to pre-amp/shaper boards and
 437 digitized and sent to the DAQ.

⁴³⁸ Chapter 4

⁴³⁹ Booster Neutrino Beam

⁴⁴⁰ Fermilab is one of the world's leading neutrino facilities and currently produces two neutrino
⁴⁴¹ beams that span a wide range of neutrino energies. The Booster Neutrino Beam (BNB),
⁴⁴² which will be described in detail throughout this chapter, is a lower energy beam that
⁴⁴³ delivers neutrinos to various short baseline experiments. Fermilab also hosts the NuMI
⁴⁴⁴ (Neutrinos at the Main Injector) Beam [] which produces neutrinos over a large range
⁴⁴⁵ between 1GeV/c-30GeV/c and delivers neutrinos to various experiments both on-axis and
⁴⁴⁶ off-axis. The NuMI beam will not be covered in this thesis.

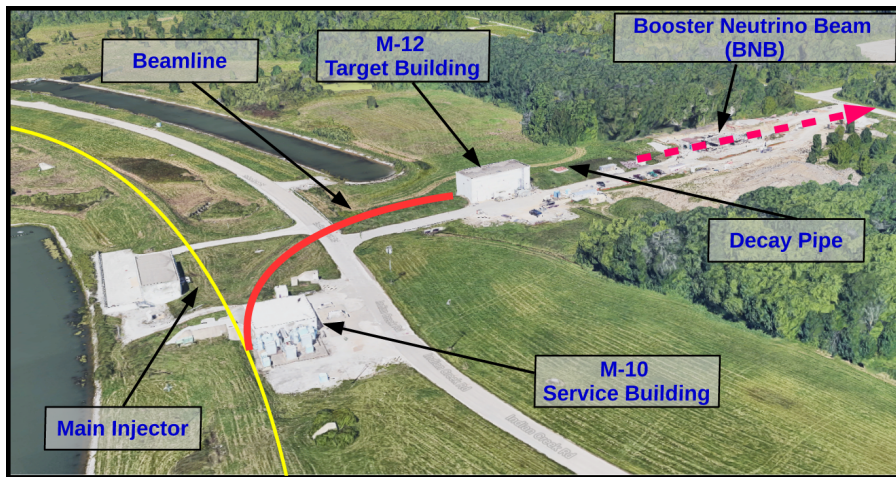


Figure 4.1: This image shows an aerial view of the Booster Neutrino Campus. Protons are extracted before the main injector near the M-10 service building and delivered to the M-12 target hall where the low energy neutrino beam is produced.

447 The Booster neutrino campus is illustrated in figure ?? . To produce the BNB, pro-
448 tons are extracted from a transfer line just prior to the main injector and then interact
449 with a beryllium target. The following sections will describe the beam system, neutrinoos
450 production process, and flux predictions for the BNB.

451 4.1 Primary Beam, Target and Horn

452 The BNB extracts 8.89 GeV/c momentum protons from the Fermilab Booster synchrotron
453 and delivers them to a beryllium target housed in the M-12 building. The protons from
454 the booster are grouped in 1.6 μ s windows called 'beam spills'. One beam spill contains
455 approximately 5×10^{12} protons. On average the Booster can run no more 5 Hz with no
456 more than 11 pulses in a row at 15 Hz. In optimal running conditions the Booster can
457 deliver 9×10^{16} protons on target (P.O.T) per hour.

458 The beam pipe directly leading to the target is approximately 5 feet long and is held
459 under vacuum to minimize proton interactions not originating from the target. The incom-
460 ing proton flux is measured by a pair of toroids which are positioned upstream of the target
461 and provide an error on P.O.T on the order of 2 %.

462 The target consists of 7 cylindrical beryllium slugs that together produce an effective
463 cylinder of 71.1 cm in length and 0.51 cm in radius. The use of multiple slugs gave the
464 beryllium more surface area to allow efficient heat transfer from a simple air cooling system
465 to be sufficient. An exploded view of the BNB target is shown in figure ?? . As the protons
466 collide with the beryllium, large amounts of secondary and tertiary mesons, such as π^\pm, K^\pm ,
467 are produced . These mesons will later decay into neutrinos and other decay particles.

468 The target is positioned inside of a large toroidal electromagnet called a horn. The horn
469 is made of an aluminum alloy (6061 T6) and is pulsed with 174 kA of current to produces
470 a $1/R$ field where R is the distance from the axis of the horn. Since neutrinos are neutral
471 particles and can not directly be focused by an electric or magnetic force. Instead, the horn
472 focuses the proper sign parent π^\pm, K^\pm in such a configuration that the neutrino angle from
473 the parent decay particles are focused in a beam.

474 Directly downstream of the horn/target assembly is a collimator that is used to reduced

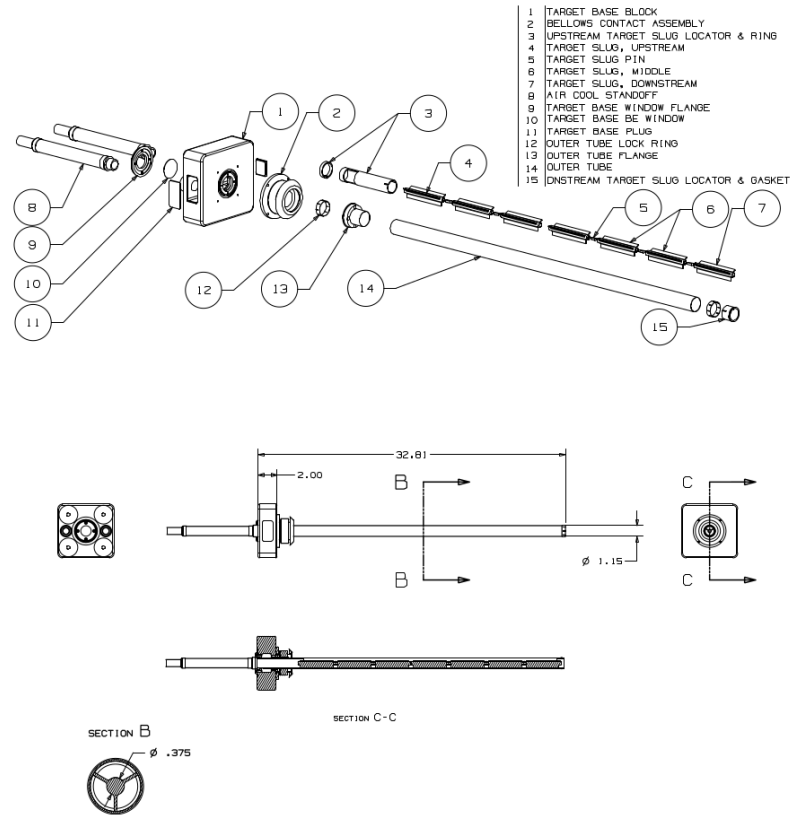


Figure 4.2: An exploded view of the BNB target which shows the 7 Beryllium slugs housed inside the support structure.

background coming from unwanted particles. Particles passing through the collimator enter a 45 m long decay region. In this region, most of the particles decay to produce the neutrino beam. At the end of the decay region there is a beam stop made of steel, concrete. There is also an array of gas proportional counters to detect high energy muons that punch through the beam stop. A diagram of the entire BNB system is shown in figure ???. When the horn polarity focuses (negative) positive charged mesons a (anti)neutrino beam is produced.

4.2 Neutrino Flux Prediction

The neutrino flux prediction for MicroBooNE uses the same GENIE simulation files used by MiniBooNE. The files are feed into a Geant4 module that simulates the particles as they

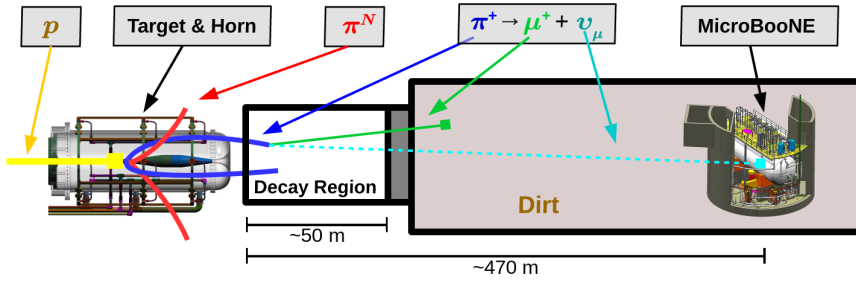


Figure 4.3: This figure shows the Booster Neutrino Beam line at FNAL. The neutrinos are produced in the decay region and then travel towards the MicroBooNE detector located 470 m down stream.

484 travel through the target, horn, and decay region. This produces a MC flux estimate for each
 485 of the various neutrino types. A systematics study was then performed to provide an error
 486 estimate for each of the ν_e , $\bar{\nu}_e$, ν_μ , and $\bar{\nu}_\mu$ flux predictions. To do this, 6 primary systematics
 487 were varied: the production rates of π^+ , π^- , K^+ , K^- , and K_L^0 , and a group systematic
 488 comprised of the horn current miscalibration, skin depth, nucleon inelastic, nucleon QE,
 489 nucleon total cross sections, pion inelastic, pion QE, and pion total cross sections. Beam
 490 errors for each of systematics are shown in Table ?? . The final flux estimate with the error
 491 uncertainty is shown in Figure ??.

	ν_μ	$\bar{\nu}_\mu$	ν_e	$\bar{\nu}_e$
Delivered P.O.T.	2.00%	2.00%	2.00%	2.00%
π^+	5.8%	0.46%	4.62%	2.66%
π^-	0.01%	7.51%	0.28%	3.20%
K^+	0.38%	0.13%	5.19%	2.61%
K^-	0.01%	0.35%	0.28%	3.92%
K_l^0	0.03%	0.27%	2.36%	22.59%
Other	5.78%	6.09%	3.6%	7.61%

Table 4.1: Systematic errors for production of various neutrino types with respect to their, P.O.T. , parent particle, and other variables.

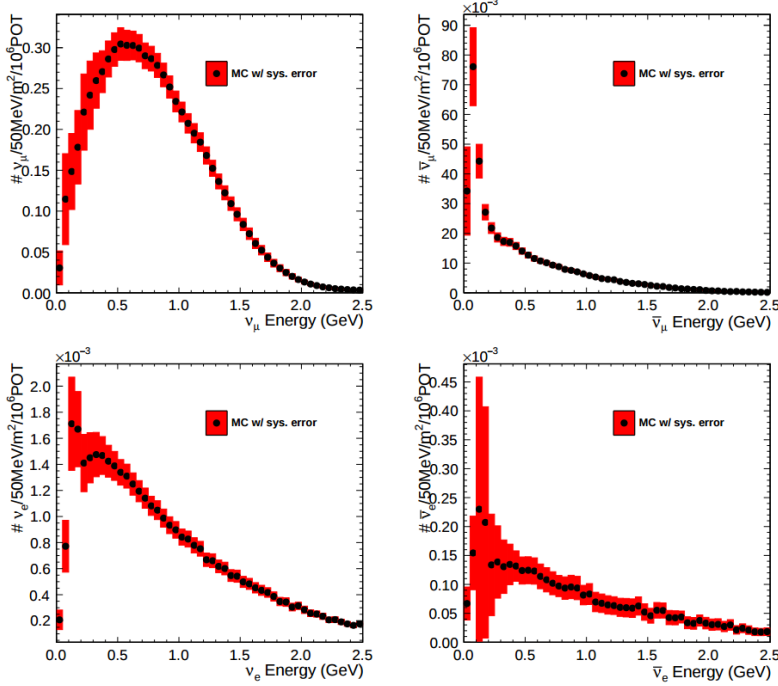


Figure 4.4: Monte Carlo flux predictions for the BNB neutrino spectrum. The red band represents the flux systematic errors. Note the orders of magnitude with the ν_μ spectrum rates.

⁴⁹² Chapter 5

⁴⁹³ Low Energy Excess and Relevant ⁴⁹⁴ Cross Sections

⁴⁹⁵ 5.1 Overview

⁴⁹⁶ This chapter will discuss various facets of what is commonly called the “MiniBooNE Low
⁴⁹⁷ Energy Excess.” First, we will present the anti-neutrino excess observed by LSND and how
⁴⁹⁸ the oscillation results can be interpreted. Then, we will discuss the efforts of MiniBooNE to
⁴⁹⁹ understand the LSND results along with their oscillation results that establish the “Mini-
⁵⁰⁰ BooNE Low Energy Excess.” We will also discuss the neutral current $1\pi^0$ cross section
⁵⁰¹ which is the dominant background in the oscillation analysis claims for both MiniBooNE
⁵⁰² and LSND. Finally, we will discuss MicroBooNE’s role towards addressing understanding
⁵⁰³ the low energy excess claims of MiniBooNE.

⁵⁰⁴ 5.2 LSND Excess

⁵⁰⁵ The Liquid Scintillator Neutrino Detector (LSND) was a 167 ton neutrino detector stationed
⁵⁰⁶ at Los Alamos National Lab (LANL) designed to study neutrino oscillations. The detector,
⁵⁰⁷ which hosted 1220 PMT’s for event detection, was place 30 m away from the source of a
⁵⁰⁸ low energy (40 MeV) $\bar{\nu}_\mu$ beam. Using the Los Alamos LAMPF beam, 800 MeV protons
⁵⁰⁹ interacted with a water target to produce π^+ mesons which decayed into $\mu^+ + \nu_\mu$. The μ^+

510 would then interact with a copper beam stop and decay at rest to produce the low energy
 511 $\bar{\nu}_\mu$ beam.

512 The detector medium was primarily carbon (mineral oil CH_2). LSND could easily
 513 distinguish between electromagnetic showers (electrons/positrons/photon) or tracks (pi-
 514 ons/muons/protons) by differences in the Cherenkov cone that was produced. The oscil-
 515 lation signal interaction was $p + \bar{\nu}_e \rightarrow n + e^+$. The primary e^+ is easily visible from the
 516 Cherenkov light it produced but a neutron will not produce Cherenkov light and therefore
 517 be invisible to the detector. The organic scintillator b-PDB was dissolved to the mineral
 518 oil at a concentration of 31 mg/l. The scintillator allowed the 2.2 MeV photon from the
 519 capture of the neutron on hydrogen to be detected. This allowed LSND a unique signal to
 520 identify $\bar{\nu}_e$ interactions. It should be noted that the detector technology could not easily
 521 discriminate between photons, electrons or positrons induced electromagnetic showers.

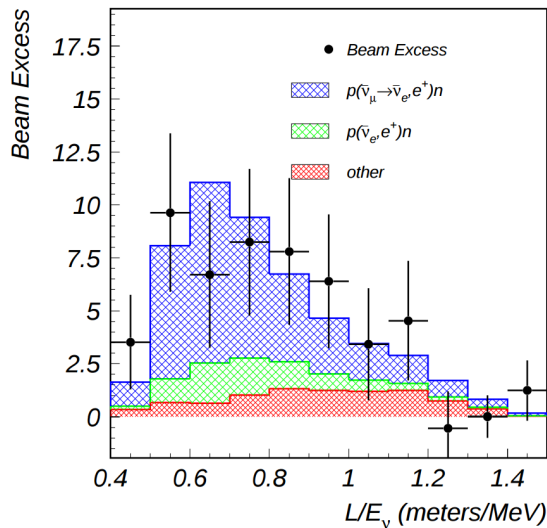


Figure 5.1: This is the LSND neutrino oscillation appearance plot as a function of L/E and represents the 87 event $\bar{\nu}_e$ excess claimed by the experiment.

522 In 2001, the collaboration published results for an observed excess of $87_{\pm 6.0}^{+22.4}$ events
 523 above the predicted background as shown in figure ???. If the excess is interpreted as
 524 neutrino oscillations from a two neutrino model, the best fit of the excess would suggest a
 525 $\sin^2(2\theta) = 0.003$ and $\Delta m^2 = 1.2\text{eV}^2$ which greatly contradicts many other measurements
 526 for $\Delta m_{2,3}^2$ or $\Delta m_{1,3}^2$ []. One explanation for the excess suggests the idea of mixing between
 527 other additional neutrino states. These neutrinos are called ‘sterile’ since they cannot
 528 directly couple via weak interaction as mentioned prior from the constraints from LEP.

529 5.3 Miniboone Excess

530 The Mini Booster Neutrino Experiment(MiniBooNE) was designed to address the claims of
 531 the LSND $\bar{\nu}_e$ excess result. The MiniBooNE detector was a mineral oil Cerenkov detector
 532 designed to be a similar technology to LSND. MiniBooNE, stationed at FNAL in the BNB,
 533 was positioned 541 m from the neutrino source and was able to receive both ν_μ and $\bar{\nu}_\mu$
 534 fluxes. The distance was chosen such that the L/E parameter were similar to that of the
 535 LSND experiment.

536 MiniBooNE, which contained 818 tons of mineral oil(CH_4), was located underneath
 537 more than 3m of earth overburden to help reduce cosmic rays. The detector supported a 35
 538 cm thick outer cosmic veto using 240 PMT’s. The veto efficiency was 99.99% for rejecting
 539 cosmic muons. The inside of the detector was instrumented with 1,280 8-inch PMT’s
 540 which were used to read out neutrino and comsic data. Cherenkov light from different
 541 particles produced distinct patterns on various PMT’s inside the spherical detector. A
 542 cartoon showing various type of signal topologies from the MiniBooNE detector are shown
 543 in figure ???. The detector energy scale was calibrated in situ by fitting various parameters
 544 from thoroughgoing muons, decay Michele electrons, and π^0 decays’s. A clear limitation of
 545 Cherenkov detectors is the inability to concretely distinguish between photon induced or
 546 electron induced showers.

547 The primary oscillation analysis for MiniBooNE was done ‘blind’ in an attempt to
 548 gain confidence from the physics community upon it’s findings. The entire analysis was
 549 developed on large statistics Monte Carlo simulation and a small sample of test data. In

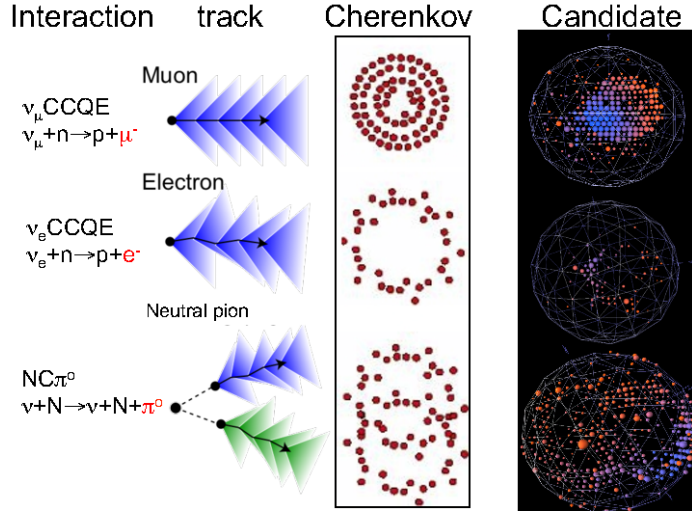


Figure 5.2: This cartoon depicts different particle interactions as observed in Cherenkov detector. The far right shows the interaction types as viewed in MiniBooNE

total, MiniBooNE accumulated 6.46×10^{20} P.O.T. of ν -data and 11.27×10^{20} P.O.T. of $\bar{\nu}$ -data. Fermilab's ability to support both neutrino and anti-neutrino beams allow for MiniBooNE to confirm that an LSND-like excess was independent of neutrino type. The data is in good agreement between signal and background predictions and contradicts the LSND claim up to 98% confidence in both modes above 500 MeV. The excess is most prominent in the region of events below 500 MeV, as seen in figure ???. In this region the largest background comes from π^0 -misidentification followed by photons coming from radiative Delta decays. MiniBooNE reports a total excess of 240.0 ± 62.9 combine $(162.0 \pm 47.8\nu, 78.4 \pm 28.5\bar{\nu})$ events in the neutrino energy range $200 < E_\nu^{QE} < 1250$ MeV. Also, if the excess is interpreted as a two flavor oscillation the inferred parameters are consistent with the LSND result.

5.4 Neutral Current π^0 production

The leading background from the MiniBooNE oscillation result, as mentioned in chapter???, is π^0 -misidentification. Accurately measuring the neutrino induced neutral current single π^0 production cross section is therefore crucial in understanding background contributions for an oscillation analysis. Charge current π^0 production conveniently has an outgoing

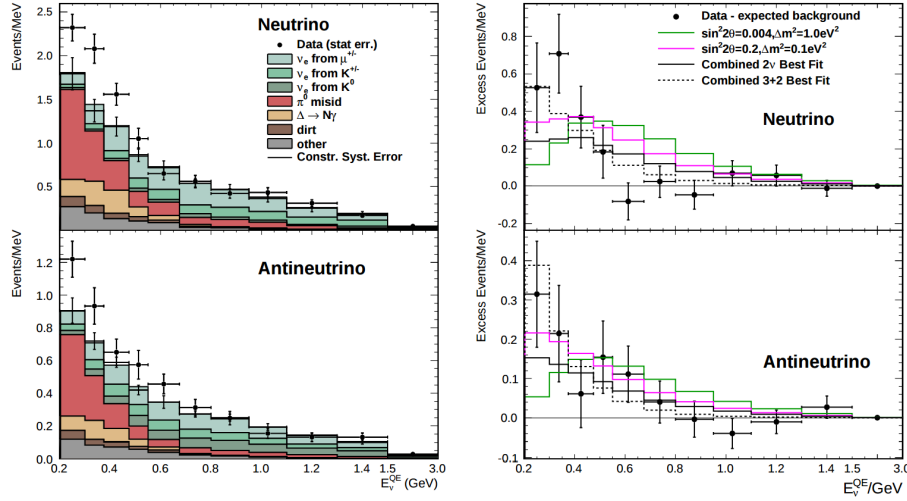


Figure 5.3: The left plots show the stacked histograms for signal and background overlaid with data for both neutrino and anti-neutrino modes. The right plots show the relative excess as a function of neutrino energy and make obvious the energy range that drives the excess.

565 charged muon in the final state and is very easy to identify. On the other hand, neutral
 566 current π^0 production does not guarantee any outgoing charged particles and therefore,
 567 makes identification much harder. For neutrinos in the BNB, the main production mode
 568 for neutrino induced neutral current π^0 production is via the $\Delta(1232)$ resonant production.
 569 Resonant production is when a baryon, such as a proton or neutron, are excited to a higher
 570 resonance state and then subsequently decays back to the initial state while liberating a
 571 π^0 . There are other neutrino induced π^0 production modes that MicroBooNE is sensitive to
 572 such as deep inelastic scattering and coherent production, but have a lower production cross
 573 section at the given BNB neutrino energy range. A general Feynman diagram can be used to
 574 describe the main components of neutrino induced neutral current single π^0 production in
 575 argon as seen in Figure ??.

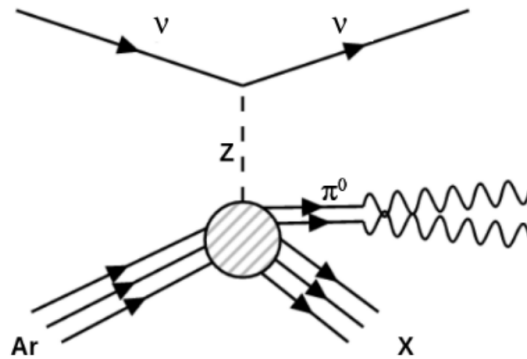


Figure 5.4: Neutrino induced single π^0 production on argon. This topology is defined such that 1 π^0 is produced and the other particles leaving the interaction (X) must only consist of nucleons.

⁵⁷⁶ 5.5 NC-Pi0 in Carbon vs Argon

⁵⁷⁷ In 2010, MiniBooNE measured the total neutral current single π^0 cross section on carbon
⁵⁷⁸ with what is currently the worlds largest statistics sample of π^0 s. The MiniBooNE neutral
⁵⁷⁹ current single π^0 signal is defined as a topology that produces one and only 1 π^0 in the
⁵⁸⁰ final state with no other other charged leptons or mesons originating from the vertex. In
⁵⁸¹ 2015, the first measurement of neutrino induced neutral current π^0 production on argon was
⁵⁸² measured by ArgoNeut collaboration at Fermilab while running in the NuMI neutrino beam.
⁵⁸³ AgroNeut, being a smaller detector, could not easily contain many of the electromagnetic
⁵⁸⁴ showers from π^0 decays. This forced the analysis choose a slightly different final state signal
⁵⁸⁵ definition requiring there to be at least one π^0 , no electron or muon, and allowing there
⁵⁸⁶ to be any number of mesons in the final state. This modified signal definition makes any
⁵⁸⁷ comparison to other historical data very complicated.

⁵⁸⁸ MicroBooNE, which resides in the same neutrino beam line as MiniBooNE, is a prime
⁵⁸⁹ candidate for various studies of neutral current π^0 production studies between different
⁵⁹⁰ target materials(C/Ar). Being a larger LArTPC, more π^0 decays will be contained allowing
⁵⁹¹ for high statistics measurements of the cross section along with the general need to measure
⁵⁹² the production rate as input to its own oscillation analysis.

593 Chapter 6

594 Cosmogenic π^0 's at MicroBooNE

595 In this chapter we will talk about some of the challenges and interesting physics cases re-
596 garding cosmogenics in a surface LArTPC. Many cosmic ray particles penetrate surface
597 detectors and populate the detector region making it necessary to remove these particles
598 from reconstruction and address charge contamination in neutrino events. The majority
599 of this chapter will emphasize cosmogenic track removal, electromagnetic showers and sub-
600 sequently π^0 selection. We will first examine some historical cosmogenic studies from the
601 Icarus experiment. Then, introduce what MicroBooNE can contribute in terms of under-
602 standing cosmics. We will address the cosmic simulation that is used, various steps in
603 reconstruction and pattern recognition used to select π^0 's in a LArTPC. Finally, we will
604 conclude with how these studies impact future cross section analyses and backgrounds to-
605 ward the low energy excess analysis.

606 6.1 Motivation

607 Cosmogenic particles allow for the separate test of reconstruction tools along with an inde-
608 pendent way to address the detector energy scale. The high rate of surface cosmics cause
609 some trouble with disentangling signal neutrino events from cosmic ray removal. Luckily, off
610 beam surface cosmogenic samples allow for a large statistics dataset to develop and optimize
611 reconstruction techniques. Cosmogenic muons that traverse the detector provide a handle to
612 understand detector energy scale along with understanding track reconstruction efficiency.

613 Stopping muons that produce a Michele electron help provide a benchmark for low energy
 614 showers in the 10's of MeV range. The π^0 resonance, with a mass of $134.9 \text{ MeV}/c^2$, can
 615 be used as a standard candle to benchmark overall detector energy scale. The calculated
 616 the π^0 mass, as shown in equation ??, depends on a measurement of energy and photon
 617 opening angle.

$$\mathcal{M} = \sqrt{2E_1E_2(1 - \cos\theta_{12})} \quad (6.1)$$

618 Electromagnetic shower reconstruction for LArTPC's is well known to be a hard task.
 619 The high resolution of the 2-dimensional projections of EM-showers introduce many chal-
 620 lenges to develop unbiased and fully automated reconstruction. In 2001, the T600 ICARUS
 621 detector ?? performed a surface test run in Pavia, Italy. During this 100 day test the detec-
 622 tor collected over 30,000 cosmic ray events. In 2008, the ICARUS collaboration published
 623 a study of electromagnetic showers coming from π^0 decays in the Pavia dataset. To select
 624 candidate π^0 events, ICARUS hand scanned a total of 7,500 potential events from a PMT
 625 triggered sample. Their hand scanning requirements included, that at least two well sep-
 626 arated electromagnetic showers were visible, a valid t_0 time for the vertex, and that there
 627 was not much charge contamination coming from a nearby cosmic muon. After this, they
 628 were left with 212 hadronic interactions with at least one candidate neutral which they then
 629 proceeded to reconstruct. Their final reconstruction consisted of energy scaling to account
 630 for missing charge in the shower and a minimization against the true π^0 mass. An example
 631 of one of their hand scanned clustering events is shown in Figure ??.

632 MicroBooNE, being a surface detector, is in a position to do a similar study with im-
 633 proved reconstruction techniques. Also, understanding the cosmic production rate for single
 634 π^0 's is valuable to any MicroBooNE analysis that involves EM-showers. The following sec-
 635 tions will present MicroBooNE's Monte Carlo simulation and state of the art reconstruc-
 636 tion techniques.

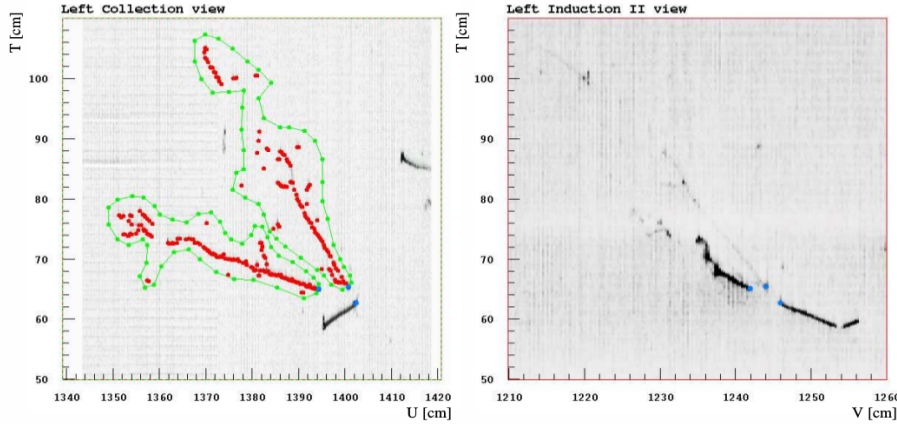


Figure 6.1: A cosmic π^0 from the ICARUS Pavia run. The left image shows the hand drawn clustering and positions of the shower conversion point and vertex point. The right image shows the same event on a different wire plane view.

6.2 Traditional Reconstruction

The traditional approach for LArTPC reconstruction involves grouping drift charges that are deposited on the wires to form wire-hits. The light collection system also has light-hits which corresponded to collected light of an individual track or shower. A group of PMT's that have light-hits at the same time is called a flash. Hits from each of the wire planes are clustered together with various reconstruction algorithms to form reconstruction objects that relate to individual particles in the detector. There are two primary reconstruction objects: tracks, which are mostly linear and compact clusters that represent muons, protons, and charged pions, and showers which are more fuzzy shaped cluster objects that represent photons and electrons. Next, to reconstruct a 3D object, an algorithm must match the same 2D cluster objects in at least two of the three wire planes. For MicroBooNE, and the general LArTPC community, matching track reconstruction is well advance but shower reconstruction suffers many hurdles. In recent years lots of progress has been made for LArTPC shower reconstruction. Various different techniques such as improved 2D clustering and matching techniques[], sophisticated pattern recognition tools[], and deep learning[] approaches have been explored and each has its various strengths and weaknesses.

653 6.3 Wire Cell Imaging

654 The traditional approach is not the only way to reconstruct LArTPC data. Instead, wire
 655 data can be treated with a tomographic approach directly producing a set of 3D space
 656 points. Although computationally intensive, this approach allows for more information to
 657 be used in a 3D clustering framework which can directly impact shower reconstruction and
 658 mitigate degeneracies from the 2D matching method.

659 The Wire-Cell framework, spearheaded by Brookhaven National Labs (BNL), utilizes
 660 this approach to create 3D space points from MicroBooNE's TPC data. The approach
 661 relies on the assumption that the same amount of ionization charge is seen on each plane.
 662 In MicroBooNE this is done by reconstructing small time slices on each wire planes. Each
 663 time slice involves solving a charge equation for all possible hits with respect to the matrix
 664 of hits actually recorded in the time slice. The charge equation is shown in equation ???. The
 665 detector wire signals are represented in matrix W while all potential wire hits are contained
 666 in H. Nonzero values in the Q matrix will correspond to unique wire-plane intersections of
 667 charge, near zero values represent ghost hits due to degeneracies in the charge equation.

$$\begin{bmatrix} W_{u_1} \\ \vdots \\ W_{u_n} \\ W_{v_1} \\ \vdots \\ W_{v_n} \\ W_{y_1} \\ \vdots \\ W_{y_n} \end{bmatrix} = \begin{bmatrix} Q_{u_1}^{H_1} & Q_{u_1}^{H_2} & \dots & \dots & \dots & Q_{u_1}^{H_{m-1}} & Q_{u_1}^{H_m} \\ \vdots & \vdots & \ddots & \ddots & \ddots & \vdots & \vdots \\ Q_{u_n}^{H_1} & Q_{u_n}^{H_2} & \dots & \dots & \dots & Q_{u_n}^{H_{m-1}} & Q_{u_n}^{H_m} \\ Q_{v_1}^{H_1} & Q_{v_1}^{H_2} & \dots & \dots & \dots & Q_{v_1}^{H_{m-1}} & Q_{v_1}^{H_m} \\ \vdots & \vdots & \ddots & \ddots & \ddots & \vdots & \vdots \\ Q_{v_n}^{H_1} & Q_{v_n}^{H_2} & \dots & \dots & \dots & Q_{v_n}^{H_{m-1}} & Q_{v_n}^{H_m} \\ Q_{y_1}^{H_1} & Q_{y_1}^{H_2} & \dots & \dots & \dots & Q_{y_1}^{H_{m-1}} & Q_{y_1}^{H_m} \\ \vdots & \vdots & \ddots & \ddots & \ddots & \vdots & \vdots \\ Q_{y_n}^{H_1} & Q_{y_n}^{H_2} & \dots & \dots & \dots & Q_{y_n}^{H_{m-1}} & Q_{y_n}^{H_m} \end{bmatrix} \begin{bmatrix} H_1 \\ H_2 \\ \vdots \\ H_{m-1} \\ H_m \end{bmatrix} \quad (6.2)$$

668 Then, each ‘slice’ is stacked to it’s corresponding x position. This produces a set of 3D
669 space points that can used in patter recognition algorithms to identify different particles
670 in the data. All reconstruction is done with accounting for known detector dead regions.
671 The current state of MicroBooNE’s signal and noise processing and imaging that requires
672 a minimum of 2 wire planes to be matched from the charge equation.

673 **6.4 Pattern Recognition**

674 Various pattern recognition tools are needed to address MircoBooNE’s TPC data but for
675 this analysis they can be generalized into two efforts, cosmic track removal and EM-shower
676 clustering. Both approaches require different techniques. First, we will focus on optimizing
677 track removal. This involves identifying tracks that are through-going, and contained. Once
678 all the charge associated with tracks are removed, the remaining charge is clustering into
679 candidate EM-shower objects. Finally, correlated shower pairs are identified and selected
680 as candidate π^0 events.

681 A image of a typical MicroBooNE cosmic event reconstructed with 3D wire cell space
682 points are shown in Figure ?? using the BEE viewer []. A detailed list of reconstruction
683 and selection parameters are listed in appendix ??

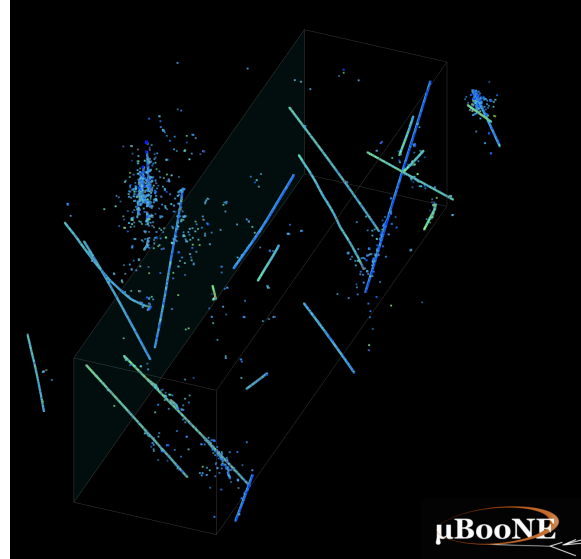
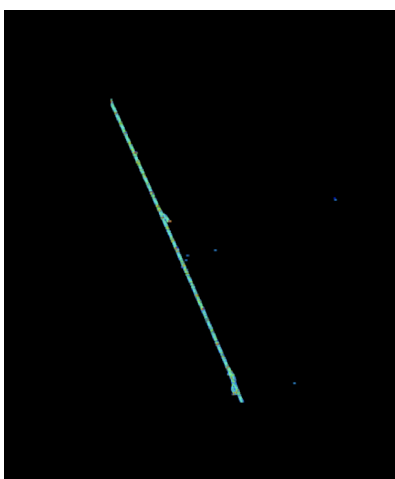


Figure 6.2: This is a typical cosmic event in the MicroBooNE detector. The data used to generate this event is CORSIKA Monte Carlo.

684 6.5 Clustering

685 The wire cell data produces a set of 3D space points as mentioned in section ???. Only space
 686 points that are in the fiducial volume are clustered and considered in the reconstruction
 687 process. First a charge threshold cut of 0.5 MeV is applied to all the remaining space points.
 688 This is to remove very low charge ghost points and reduce the overall number of points to
 689 cluster. The main goal of this step is to identify the large scale structure of the cosmic
 690 tracks in the data. Additionally, with a smaller number of space points the computational
 691 time for reconstruction is reduced.

692 The first stage of clustering uses BIRCH (balanced iterative reducing and clustering
 693 using hierarchies). The hyper parameters were tuned such that cosmic tracks are removed
 694 with minimal impact to showers involved from π^0 . Birch clustering was chosen because it
 695 scales well with large number of points, efficiently maintains large number of clusters in
 696 datasets and also handles outliers removal well. This clustering technique leverages on the
 697 inherent structure of charged particle tracks having a well define 3-dimensional trajectory.
 698 Particles such as protons, muons, and charged pions are continuously ionizing meaning
 699 that there should be not be gaps in the detected charge. This feature is much different than



(a) This figure shows an image of muon track as viewed from the BEE-WireCell image viewer.



(b) This figure shows an image of $\pi^0 \rightarrow \gamma\gamma$ decay as viewed from the BEE-WireCell image viewer.

700 EM-showers which have lots of gaps between detected charge. An example of this is shown
701 in figure ??

702 The next stage of the track and shower clustering process is to merge together proto-
703 clusters that did not get fully grouped together in the BIRCH clustering step. The second
704 pass clustering is geared toward larger object clustering. To address this, a 3D convex hull
705 is constructed around every cluster. Next, the euclidean distance between all the vertex
706 points are calculated. If the minimum merging distance is small, as it is for many charge
707 particle tracks, the clusters get merged together well. Clusters from showers, as they tend
708 to be very spread out, still need further merging.

709 The final stage of clustering is shower clustering. This requires there to be a distinction
710 between a cluster object that is shower-like or track-like. To do this, parameters that
711 describe various aspects of a cluster are calculated. The most important features from
712 the cluster parameters are cluster length and spread of the first principle component. More
713 details about track and shower selection are described later in section ??.

714 Once defined as a shower cluster, a 3D charge weighted axis is fit to the cluster's set
715 of space points. First, a distance of closest approach (DOCA) for each cluster axis pair
716 is calculated and a proto-vertex is calculated at the midpoint of the DOCA line. Next, a

unique conversion point is calculate for each shower pair to identify the start point of the shower. This can also be thought of as a proxy for the photons conversion point. Using the proto-vertex point and two conversion points an opening angle is calculated. A pair of clusters that have a DOCA that is less than 5 cm, an angle between 15 and 165 degrees, and both of the conversion lengths are less than 20 cm are merged together. The merging is done for all shower cluster pairs as a final stage of the merging process.

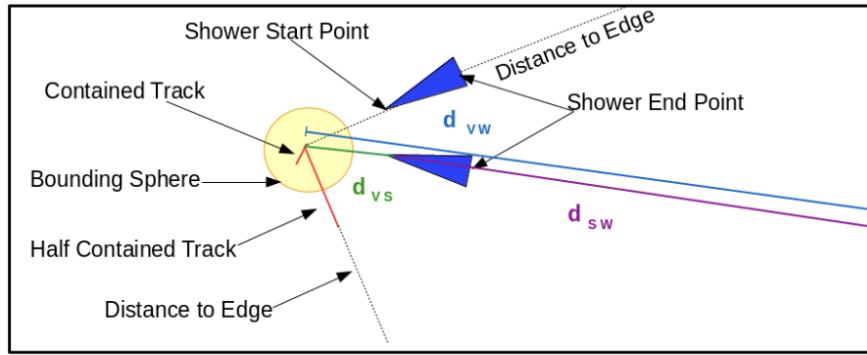


Figure 6.3: This graphic illustrates all the data objects and relevant parameters. The shower objects are shown in blue, track objects shown in red, and a bounding sphere, used to associate tracks with the vertex, is shown in yellow.

6.6 Track and Shower Selection

6.6.1 Track Removal

For this analysis track removal is handled in a unique manner. The primary goal is to identify showers coming from a π^0 . Therefore, all cuts and optimizations will be tested against shower objects. Being that we simply are trying to identify charged tracks and not particle type, the charge information is not used. The general approach for track removal depends heavily on geometric properties such as length and linearity of the cluster.

730 **6.6.2 Single π^0 Reconstruction**

731 The vast majority (98.8%) of π^0 's decay into two photons. The relationship for the par-
 732 ticle mass, which was defined in eq ??, shows the importance of properly accounting for
 733 the energy and angle between the decay photons. To understand a baseline for reconstruc-
 734 tion efficiency we have generated a sample of 10,000 single particle π^0 events isotropically
 735 throughout the detector volume with initial momenta spanning from 0 to 2 GeV.

736 First we will investigate energy deposited in detector from the decay. An plot of the true
 737 kinematic energy of photons from the decay particle is shown in Figure ???. It is important
 738 to note that both photons need to be reconstructed to form a mass. This means that we
 739 are driven to optimize the reconstruction to be robust around showers in the range of many
 740 10's of MeV in deposited energy. Photons that convert near the fiducial edge of the detector
 741 can escape and deposit only a small amount of energy in the detector. This poses problems
 742 for capturing the total amount of energy of the shower and drives the need for a fiducial
 743 cut around the edges.

744 To understand the reconstruction accuracy for the energy we are most interested in two
 745 metrics. The first is the total collected energy deposited by the two showers. This informs
 746 us that we are accounting for most of the energy deposited and handling the fiducial cuts
 747 well. The second is the product of the two shower energies. This directly impacts the
 748 reconstructed mass resolution and informs us that we are clustering energy between the
 749 two showers properly. In figure ?? both metrics are plotted for reconstruction against true.
 750 Points along the diagonal would represent accurate model predictions. As we will see later
 751 in this chapter, the energy product drives the width of the mass resolution.

752 Next we will investigate the effects of the opening angle between the two photons.
 753 The minimum opening angle of the photons is constrained by the momentum boost as
 754 the particle decays as shown in equation ???. The angular resolution is a very challenging
 755 problem in LArTPC's using the traditional 2D projection approach. Fortunately, direct
 756 3D reconstruction improves the angular resolution and allows for a better measurement of
 757 shower direction.

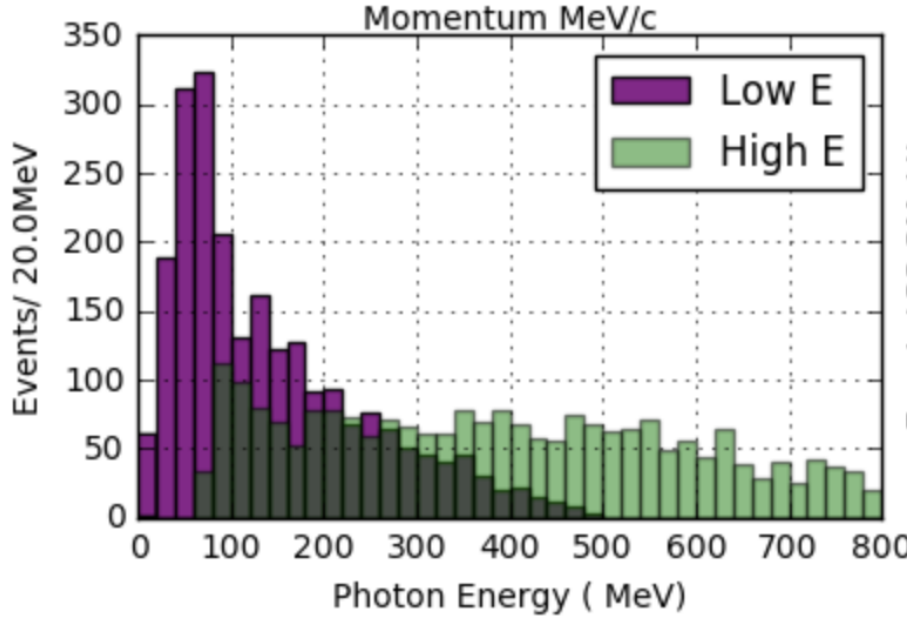
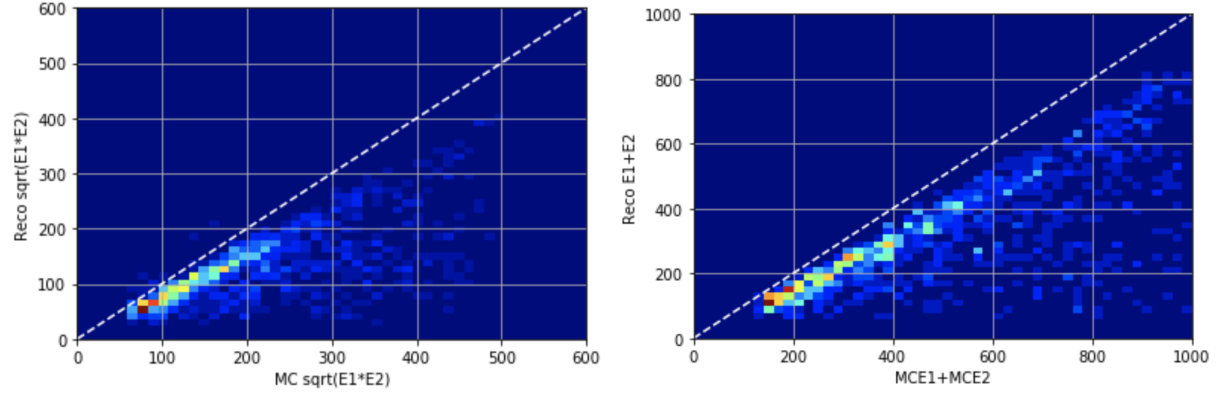


Figure 6.4: This figure shows the photon distribution for π^0 decays from a single particle sample of between 0-2 GeV. The higher energy photon is shown above in green along with the corresponding lower energy photon shown in magenta.

$$\sin \frac{1}{2}\theta_{min} = \frac{M}{E_{\pi^0}} \quad (6.3)$$

758 A plot of the reconstructed vs true opening angle is shown in Figure ???. The $1 - \cos\theta$
759 term from equation ?? is sensitive to tails of the mass distribution.

760 Next, we apply a final set of selection cuts. First, we require that the distance of closest
761 approach between the two shower axis is less than 5 cm. This is to help ensure that the
762 photons are originating from a common origin. Next, the photon conversion distance can
763 not be longer than 70 cm. This is done to help identify showers that are correlated from
764 the same decay. Finally we only accept showers that are above 50 MeV in reconstructed
765 energy. Figure ?? shows the effect of various parameters as applied to the reconstruction.
766 We find that the deficit in mass peak is mainly due to the energy reconstruction. This is
767 due to the missing energy during clustering. For this analysis there is also an additional
768 component of energy missing since we will not be using the initial t_0 -tag. The t_0 -tag is



(a) Scatter plot of reconstructed energy sum vs true energy sum
(b) Scatter plot of reconstructed energy product vs true energy product

Figure 6.5: Reconstructed energy sum and energy product for shower pairs. Both, the reconstructed energy sum and product is less than the true energy deposited.

used to identify how far the electrons had to drift to reach the wire plane. Without using t_0 , there is no effective way to correct back for electron drift effects. Thankfully, this effect is can be captured in understanding the distribution of reconstructed mass peak in the Monte Carlo.

Finally, we address the over all efficiency for reconstruction. The average reconstruction efficiency between 0 and 1 GeV/c is 40.1%. The reconstruction efficiency is shown in Figure ???. As can be seen there, the efficiency drops at low and high energies. At low momentum the π^0 's are produced nearly at rest with both showers having similar energies. Most importantly the showers are produced nearly back to back. Without having a well defined vertex, sometime the reconstruction will identify the angle as being close to zero. Being that there is a minimum opening angle cut some of the events are lost from this effect. At high momentum, many of the showers are boosted to small opening angle which we see a similar effect in the loss of efficiency.

6.7 Single π^0 cosmic sample

The MicroBooNE cosmics Monte Carlo is generated by CORSIKA(COsmic Ray Simulation for Kascade) v-7.4003[?] CORSIKA simulates particles coming from a wide range of

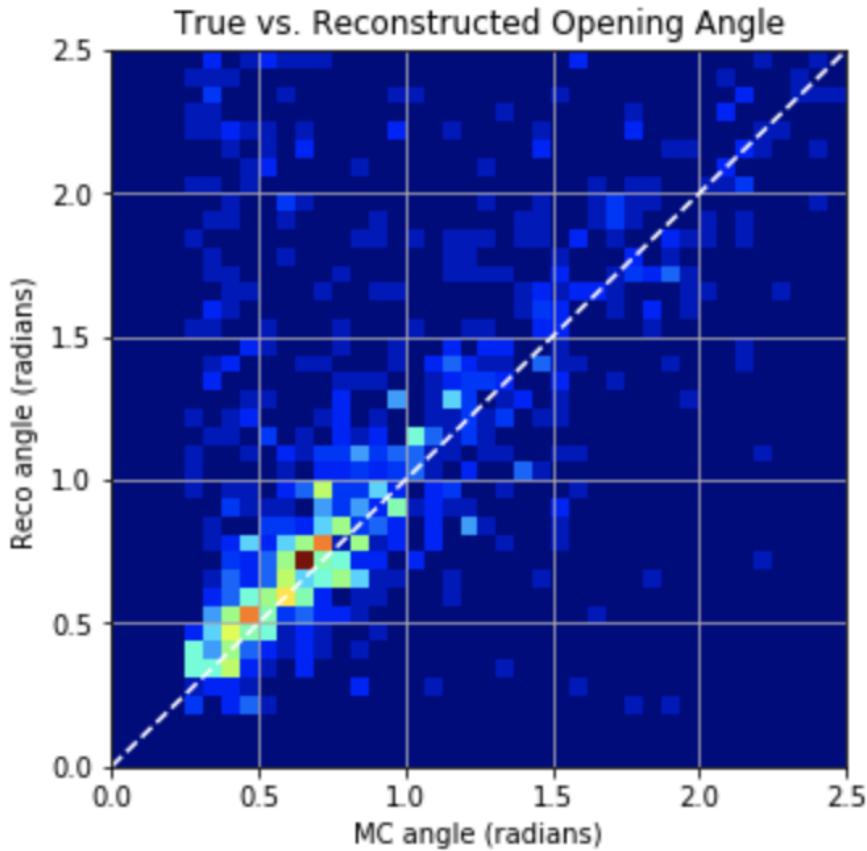


Figure 6.6: This scatter plot shows the reconstructed opening angle vs. true opening angle. We see that the reconstruction does very well with reconstructing this quantity due to the use of wire-cell's 3D approach. When the reconstruction performs badly it tends to identify small opening angles as large ones since we are not using any vertex information.

interactions initiated by cosmic ray particles in the upper atmosphere. The simulation is robust and accounts for various input parameters such as, longitude and latitude, elevation, and the earth's magnetic field. The particles are simulated over a large region above the detector complex but only particles that travel through the detector cryostat volume are kept. The passage of these particles simulated by the GEANT4 package. Cosmic rays that do not travel through the cryostat have a low likelihood of producing secondary or tertiary particles that enter the detector TPC volume [?]

In one MicroBooNE drift window (2.3ms) there are on average 6 cosmic muons. The

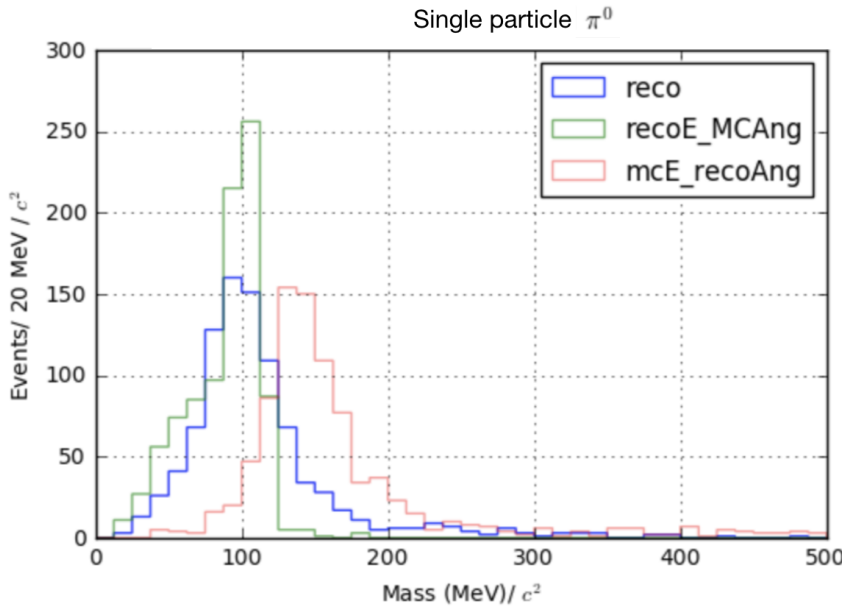


Figure 6.7: The reconstructed mass distribution is shown to highlight effects from reconstruction. First, in blue, the full reconstructed mass is shown. Second, in green, the reconstructed mass is calculated using the true angle. Third, in red, the reconstructed mass is calculated using the true energy.

793 muons do not directly contribute to many EM-showers but sometimes pass through an EM-
 794 shower from another particle. For MicroBooNE, the vast majority of muons are through
 795 going and do not lead directly to any method of π^0 production.

796 Various other particles such as, protons, neutrons, and charged pions enter the TPC
 797 volume and may produce π^0 's. A distribution of π^0 production process is shown in Figure
 798 ???. Nearly half of the π^0 's produced in the MicroBooNE TPC are produced through neutron
 799 inelastic scattering.

800 In total, 90,297 CORSIKA truth events were produced to constrain production rates for
 801 signal and background. From that, a random sample of 10K events were ran through the
 802 wire-cell imaging reconstruction. Additionally, a signal sample of events contains a single
 803 neutron π^0 of $\approx 1.2K$ was produced and reconstructed through the wire-cell imaging. The
 804 exact rates will be discussed in Chapter 7.

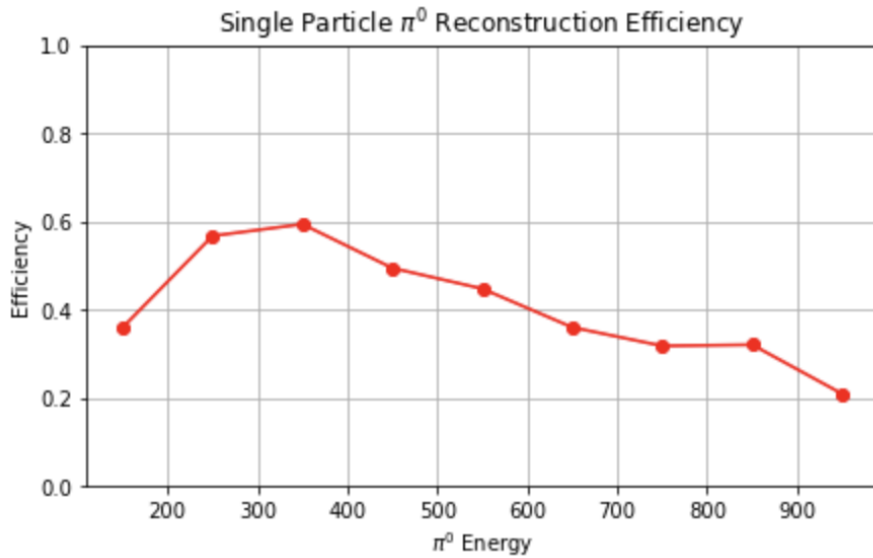


Figure 6.8: The plot shows the π^0 reconstruction efficiency for π^0 's over a 1000-10,000 MeV energy range. The reconstruction efficiency peaks around 350 MeV which conveniently is around the production energy for cosmic π^0

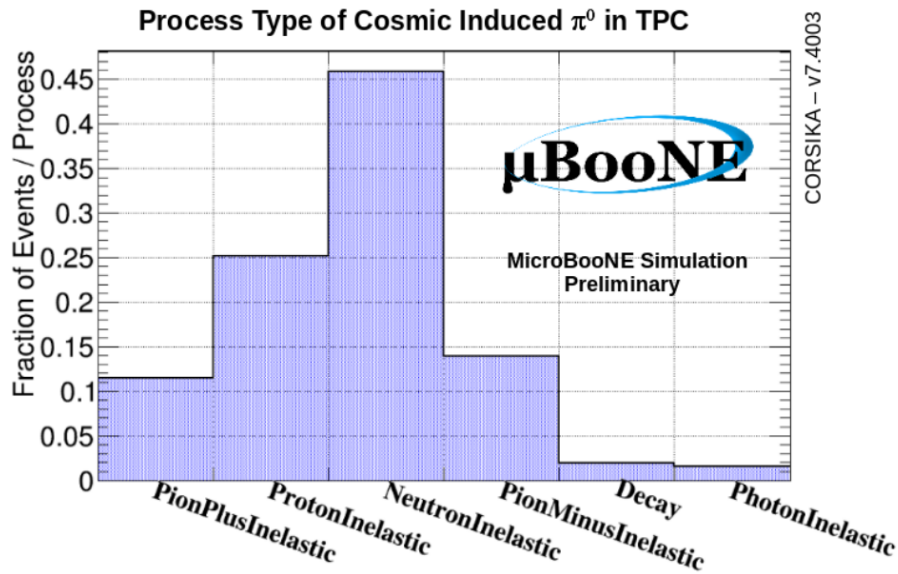


Figure 6.9: Physical process for cosmic π^0 that decay inside the TPC.

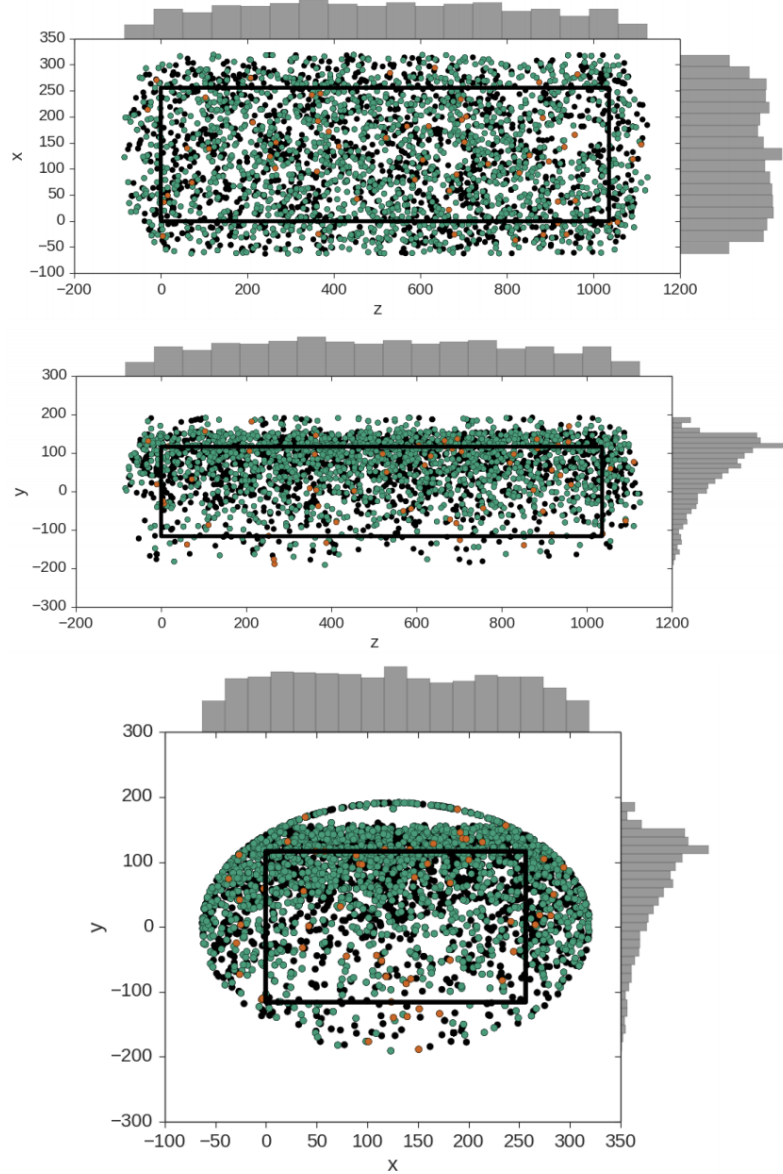


Figure 6.10: These plots show the decay point of actual cosmic π^0 's throughout any time in the 4.8 ms window. The green points represent neutron induced π^0 's, the orange represent photon induced π^0 's, and the black represent a π^0 that was produced from a charged particle. In each plot the black box is to represent the entire TPC dimensions not including fiducial cuts. Note that this is a stacked scatter plot with ordering; charged particle(black), photon(orange), neutron(green).

805 Chapter 7

806 Results

807 The goal of this study primarily two fold. The first goal is to highlight a different technique
808 to reconstruct π^0 and EM-showers in an LArTPC. To best showcase this reconstruction
809 technique we will focus on reconstructing π^0 's that are induced from a single neutron. In
810 many instances, neutral induced interactions do not have a vertex. Reconstructing EM
811 showers from a π^0 decay without a vertex poses many challenges for traditional techniques.
812 The Wire-Cell imaging approach allows for a full 3D shower reconstruction without the use
813 of a vertex. The second goal is to measure and compare the cosmic ray neutron induced
814 $1-\pi^0$ production rate in the MicroBooNE detector. This reconstruction technique is well
815 suited for this type of analysis.

816 This section will address results from both Monte Carlo and actual MicroBooNE cosmics
817 data. To be clear, we will define our signal to be events that produce 1 and only 1 neutron
818 induce single π^0 inside the TPC fiducial volume. For this analysis the fiducial volume is
819 defined from: X [0,256] , Y[-116,116], Z[400,800]. We also restrict our bounds to events that
820 happen in 1 drift window as defined in section ??

821 7.1 Monte Carlo Simulation

822 First, a word on simulation constraints. While the wire-cell imaging process provides consid-
823 erable gains towards extracting high resolution LArTPC reconstruction, it does come with
824 a high computational cost. This was an issue for generating a large sample of Monte Carlo

Table 7.1: Cosiska MC rates

Neutron induced 1 π^0	1,255
Neutron induced 1 π^0 outside	13,434
Proton induced 1 π^0 outsize	5,038
Other induced 1 π^0	9,530
no 1 π^0 or multi π^0	61,040

for Wire-Cell imaging. The process should be able to be distributed, but for this analysis it this process was not yet available. This required us to use an upsampling technique with the background Monte Carlo sample which is describe in the subsequent paragraphs.

First a enhanced sample of 1,255 signal events were generated from CORSIKA, processed through wire-cell imaging, and reconstructed with the described process in section 6. A background only sample, consisting of 8,720 randomly sampled background events were processed through processed through wire-cell imaging and the reconstruction. This number was then scaled by 0.0139 to obtain an absolute background value relative to the enhanced signal sample. This scaling represents a new total of 90,297 events. One event corresponds to 1 MicroBooNE readout frame.

From the total sample we find that 1.39% are signal. The remaining background is divided into 5 categories: 1. proton induced events that produce 1 π^0 either inside or outside the fiducial volume, 2. neutron induced events that are produced outside the fiducial volume , 3. Events that produce 1 π^0 either inside or outside the fiducial volume not coming from a proton or neutron, 4. Multi π^0 produced either inside or outside the fiducial volume, 4. Events that do not contain any π^0 . Table ?? shows the corresponding counts from the 90,297 CORSIKA sample.

Next, the selection cuts described in chapter 6 are applied to both the signal sample. There are a total of 443 events that pass the cuts made in section 6. This corresponds to a signal efficiency of 35.9%. A plot for the reconstructed mass is shown in figure ???. The mass peak, which is supposed to be around $135 \text{ MeV}/c^2$, is centered around $100 \text{ MeV}/c^2$ due to the missing energy. This is in agreement with what we expect from the single particle π^0 studies from section 6.

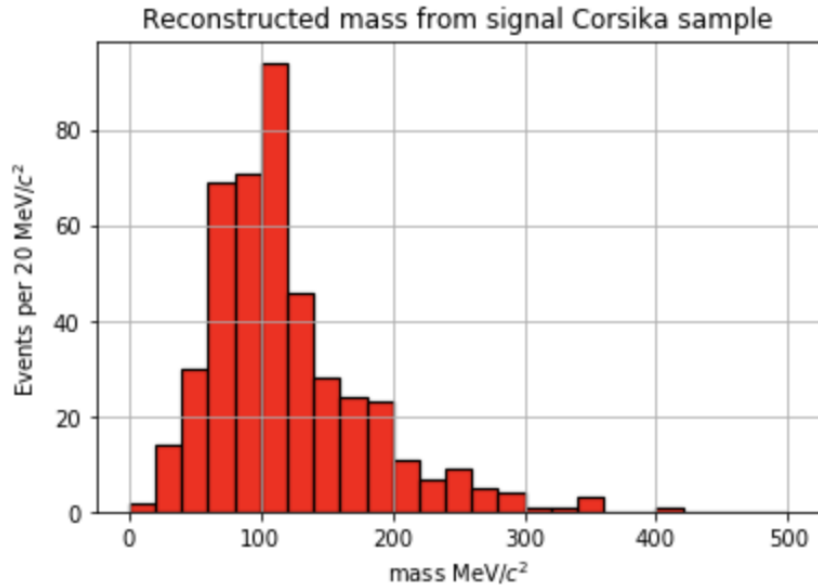


Figure 7.1: Plot of the mass distribution for neutron induced signal signal events.

848 Then, the same cuts were applied to the background only sample. We find there to be
 849 a background rate of 2.3%. Ultimately resulting in a signal:background of 0.21 (Approximately
 850 1 : 5.6). A plot of the reconstructed mass distribution for the entire background is
 851 shown in figure ??

852 It is important to note that the background distribution will also contain π^0 events. The
 853 background distribution as described in section 7.1 is plotted in figure ?? The distribution
 854 should also have some well reconstructed π^0 . For this analysis, since we did not require the
 855 use of a vertex there is a sizable portion of background that are actual reconstructed π^0 . This
 856 comes from two primary effects both of which are products of how the reconstruction criteria
 857 is defined. The first effect is part of the group coming from events with No π^0 group. Many
 858 of the events are actual π^0 particles but reconstructed out side of the fiducial volume.
 859 The second effect is in the remaining π^0 groups which obviously contains at least one
 860 π^0 . Being that we remove as many track as possible, Many proton and charged pion tracks
 861 are removed. The in eyes of the selection process a proton or charged pion induced π^0 event
 862 has a near identical topology to the signal.

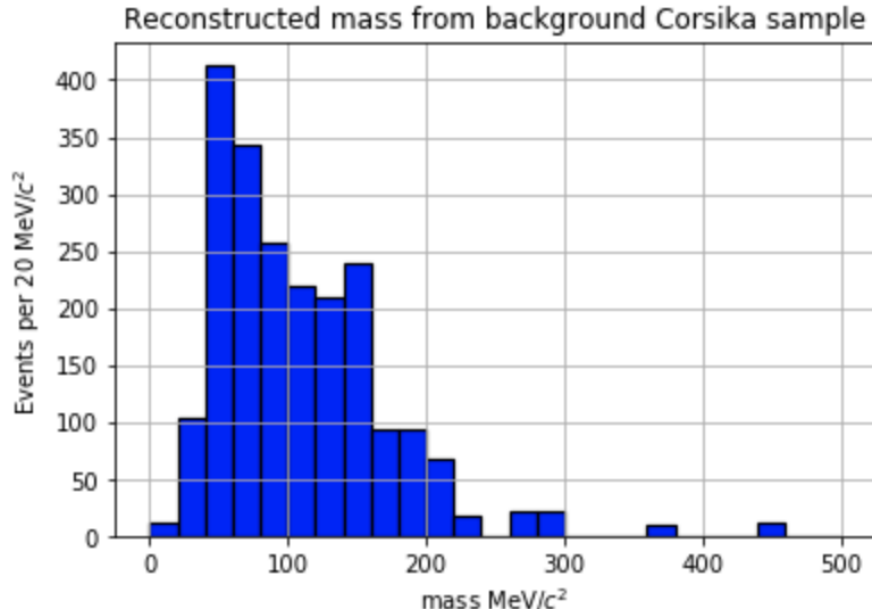


Figure 7.2: Plot of the mass distribution for cosmic background events.

863 7.2 Data

864 The same selection cuts were applied to a dataset of 13,022 off beam cosmic data events
 865 that were sampled from the 'MicroBooNE Good Run List'. This is an internal list that
 866 MicroBoone generates to define when the detector is in acceptable running mode. This list
 867 takes into account various aspects of the detector such as; wire stability, argon purity, PMT
 868 response, etc. It is important to note that the data sample that is used in this thesis is only
 869 from the good run list. Doing this, assumes that any bias in the sample is averaged over
 870 for interaction type. The mass distribution is calculated from the given 13,022 sample and
 871 there is a clear mass peak from the π^0 's that is also centered below the actual $135 \text{ MeV}/c^2$
 872 mass.

873 7.3 Data-Monte Carlo Comparison

874 To better understand the data distribution, we first plot an area normalized histogram for
 875 Monte Carlo and Data. This is shown in figure ???. We see that the shape is indeed similar
 876 but not ideal. The lack of smoothness in the Monte Carlo is due to the upsampling. Given

877 this, the area normalized shape comparison only serves the purpose of showing that we
 878 believe we are reconstructing π^0 's and reasonably handling the background.

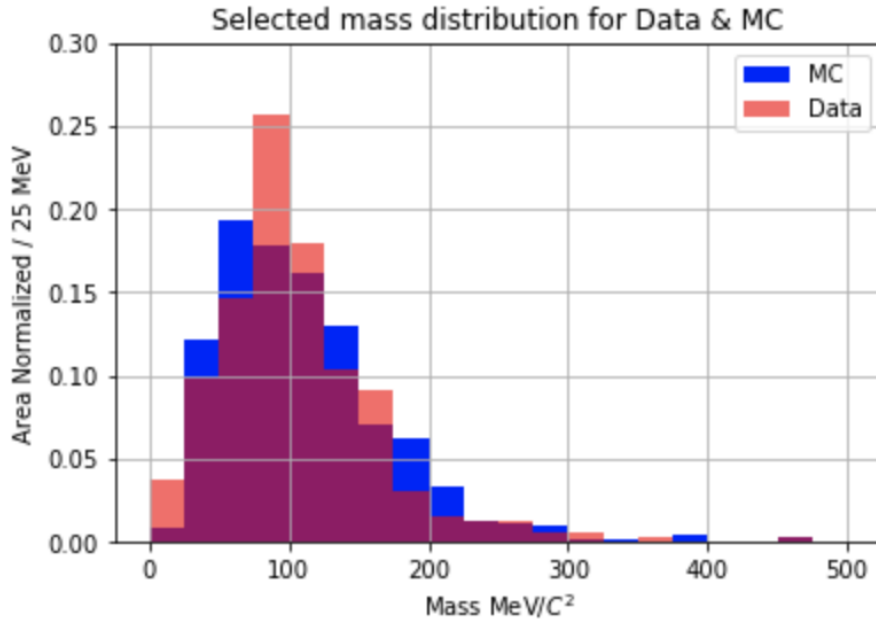


Figure 7.3: Area normalized Data-Monte Carlo mass distributions. The shapes between the data and Monte Carlo distributions provide confidence that we are reconstructing π^0 's in the distribution.

879 To better compare data and Monte Carlo an absolute rate comparison should be made.
 880 This will address how well the Monte Carlo represents the data. The mass distribution is
 881 shown in Figure ???. Out of the box, Corsika slightly over predicts the rate from data. To
 882 address this, a χ^2 minimization can be performed fit the Monte Carlo to the data. Both the
 883 signal and background are varied to optimize the fit to data. We find that the fit returns
 884 a minimum of $20.3 \chi^2/df$ when the signal is reduced by 72% and the background is also
 885 reduced by 84%. The adjusted mass distribution from the fit is shown in Figure ??

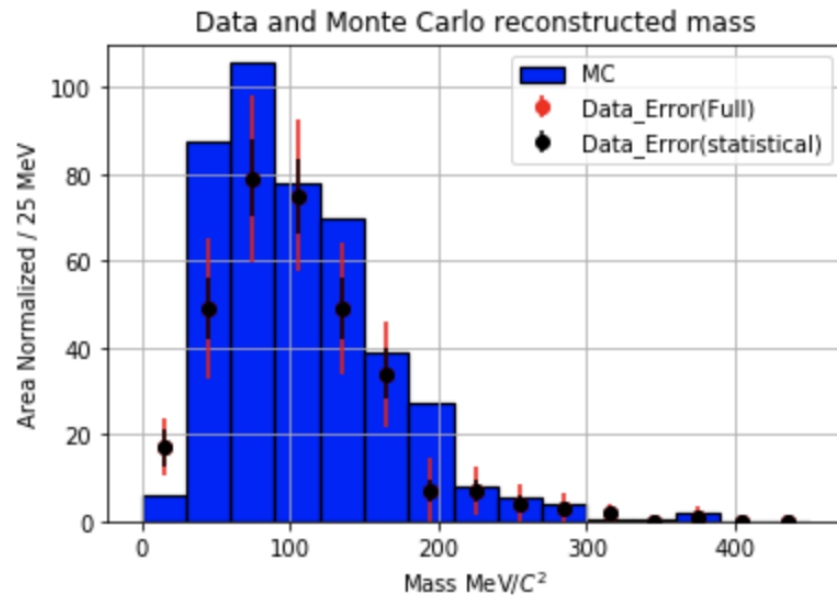


Figure 7.4: This plot shows the mass distribution from data with respect to the unchanged Monte Carlo.

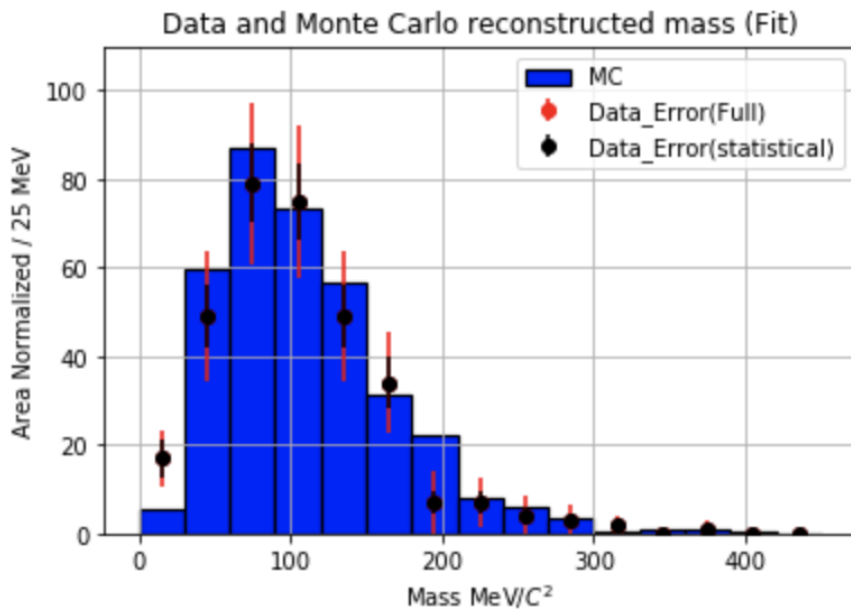


Figure 7.5: This plot shows the mass distribution from data with respect to the fitted Monte Carlo.

886 Chapter 8

887 Conclusions

888 8.1 Conclusion

889 The construction of MicroBooNE is an essential step forward for the low energy neutrino
890 physics community. The R&D process provided valuable insights towards future LArTPC
891 detector technology. The MicroBooNE detector was completed in 2015 and has since been
892 collecting valuable data.

893 This thesis showcases a radically new technique for 3D reconstruction of EM showers.
894 Although wire-cell does require a high amount of computational resources, the improved
895 3D reconstruction capabilities for EM showers provide justification. Additionally, we are
896 able to reconstruct π^0 's without the use of vertex information. We have built an algorithm
897 to identify neutron induced single π^0 events. We found that the current CORSIKA Monte
898 Carlo slightly over predicts the rate of neutron induced π^0 in the MicroBooNE detector. The
899 data used in this thesis is entirely on cosmic ray data but the extension to neutral current
900 single π^0 interaction is the next logical step.

Part I

901

Appendices

902